

1 **Regulatory myeloid cells paralyze T cells**
2 **through cell-cell transfer of the metabolite methylglyoxal**

3 Tobias Baumann¹, Andreas Dunkel², Christian Schmid³, Sabine Schmitt⁴, Michael Hiltensperger⁵, Kerstin
4 Lohr¹, Viktor Laketa⁶, Sainitin Donakonda¹, Uwe Ahting⁷, Bettina Lorenz-Depiereux⁸, Jan E. Heil⁹, Johann
5 Schredelseker¹⁰, Luca Simeoni¹¹, Andreas Fecher¹², Nina Körber¹³, Tanja Bauer¹³, Norbert Hüser¹⁴, Daniel
6 Hartmann¹⁴, Melanie Laschinger¹⁴, Kilian Eyerich¹⁵, Stefanie Eyerich¹⁶, Martina Anton¹, Matthew
7 Streeter¹⁷, Tina Wang¹⁸, Burkhard Schraven¹¹, David Spiegel^{17,19}, Farhah Assaad²⁰, Thomas Misgeld¹², Hans
8 Zischka^{4,21}, Peter J. Murray²², Annkristin Heine^{23,24}, Mathias Heikenwälder²⁵, Thomas Korn⁵, Corinna
9 Dawid³, Thomas Hofmann^{2,3}, Percy A. Knolle^{1,26,27}*† & Bastian Höchst²⁶*†

10 **Affiliations:**

11 ¹Institute of Molecular Immunology & Experimental Oncology, Klinikum rechts der Isar, School of Medicine,
12 Technical University of Munich (TUM), Germany

13 ²Leibniz-Institute of Food Systems Biology at the TUM, Germany

14 ³Chair of Food Chemistry and Molecular Sensory Science, TUM, Germany

15 ⁴Institute for Toxicology and Environmental Hygiene, School of Medicine, TUM, Germany

16 ⁵Department of Experimental Neuroimmunology, Klinikum rechts der Isar, School of Medicine, TUM, Munich,
17 Germany.

18 ⁶Department of Infectious Diseases, German Center for Infection Research (DZIF), University Heidelberg, Germany

19 ⁷Institute of Human Genetics, Stoffwechsel-Zentrum, Klinikum rechts der Isar, School of Medicine, TUM, Germany

20 ⁸Institute of Human Genetics, Helmholtz Zentrum München, Munich, Germany

21 ⁹Carl Zeiss Microscopy GmbH, Göttingen, Germany

22 ¹⁰Walther Straub Institute of Pharmacology and Toxicology, Faculty of Medicine, Ludwig-Maximilians-Universität
23 München, Munich, Germany

24 ¹¹Institute of Molecular and Clinical Immunology, Otto-von-Guericke University, Magdeburg, Germany

25 ¹²Institute of Neuronal Cell Biology, TUM, Munich Cluster for Systems Neurology and German Center for
26 Neurodegenerative Diseases, Munich, Germany

27 ¹³Institute of Virology, Helmholtz Zentrum München, Munich, Germany

28 ¹⁴Department of Surgery, Klinikum rechts der Isar, School of Medicine, TUM, Germany

29 ¹⁵Department of Dermatology and Allergy, TUM, Germany

30 ¹⁶ZAUM-Center of Allergy and Environment, TUM and Helmholtz Center Munich

31 ¹⁷Department of Chemistry, Yale University, New Haven, USA

32 ¹⁸Broad Institute of Harvard & MIT, Cambridge, USA

33 ¹⁹Department of Pharmacology, Yale University, New Haven, USA

34 ²⁰Botany, Plant Science Department, Centre for Life Science, TUM, Germany

35 ²¹Institute of Molecular Toxicology and Pharmacology, Helmholtz Center Munich, Neuherberg, Germany.

36 ²²Max-Planck Institute for Biochemistry, Martinsried, Germany

37 ²³Medical Clinic III for Oncology, Hematology and Rheumatology, University Hospital Bonn, Germany

38 ²⁴Institute of Experimental Immunology, University Bonn, Germany

39 ²⁵Division of Chronic Inflammation and Cancer, German Cancer Research Center (DKFZ), Heidelberg, Germany

40 ²⁶Institute of Molecular Immunology, School of Life Sciences, TUM, Munich, Germany

41 ²⁷German Center for Infection Research, Munich Site, Germany

42 *† these authors contributed equally and serve as corresponding authors

43
44 Address for correspondence

45 Bastian Höchst, PhD

46 Institute of Molecular Immunology, TUM School of Life Science, Weihenstephan, Alte Akademie 8, 85354 Freising, Germany
47 & Percy A. Knolle, MD

48 Institute of Molecular Immunology and Experimental Oncology, TUM School of Medicine, Ismaningerstr 22, 81675 München,
49 Germany, and TUM School of Life Science, Weihenstephan, Alte Akademie 8, 85354 Freising, Germany

50 Tel: +49 89 4140 6920

51 e-mail: Bastian.Hoechst@tum.de & Percy.Knolle@tum.de

52 **Abstract**

53 Regulatory myeloid immune cells, such as myeloid-derived suppressor cells (MDSCs), populate
54 inflamed or cancer tissue and block immune cell effector functions. Lack of mechanistic insight
55 into MDSC suppressive activity and a marker for their identification hampered attempts to
56 overcome T cell-inhibition and unleash anti-cancer immunity. Here we report that human MDSCs
57 were characterized by strongly reduced metabolism and conferred this compromised metabolic
58 state to CD8⁺ T cells thereby paralyzing their effector functions. We identified accumulation of
59 the dicarbonyl-radical methylglyoxal, generated by semicarbazide-sensitive amine oxidase
60 (SSAO), to cause the metabolic phenotype of MDSCs and MDSC-mediated paralysis of CD8⁺ T
61 cells. In a murine cancer model, neutralization of dicarbonyl-activity overcame MDSC-mediated T
62 cell-suppression and together with checkpoint inhibition improved efficacy of cancer immune
63 therapy. Our results identify the dicarbonyl methylglyoxal as marker metabolite for MDSCs that
64 mediates T cell paralysis and can serve as target to improve cancer immune therapy.

65 Introduction

66 Immune surveillance against infection and cancer relies on the appropriate induction of immune
67 cell effector functions in peripheral tissues¹. The mechanisms determining activation of innate
68 immune cells such as monocytes or macrophages through immune sensory receptors or
69 cytokines, and of adaptive immune cells such as T cells through the cell receptor and
70 costimulatory signals have been well characterized². However, regulatory or inhibitory
71 mechanisms that control immune cell function, in particular CD8⁺ T cell effector functions are
72 increasingly recognized as key determinants for the outcome of immune responses in peripheral
73 tissues^{3, 4}. The discovery of co-inhibitory molecules on T cells such as programmed cell death
74 protein 1 (PD-1) as checkpoints of immunity has opened new avenues for targeted immune
75 intervention to reconstitute tumor-specific T cell immunity in several cancer entities⁵.
76 Furthermore, regulatory immune cell populations responsible for such control of T cell effector
77 functions and their suppressive mechanisms have been intensively studied. Identification of
78 Foxp3 as key transcription factor determining induction of regulatory CD4⁺ T (T_{reg}) cells⁶ paved
79 the way to elucidate the molecular mode-of-action as to how these T_{reg} cells controlled effector
80 CD8⁺ T cell functions⁷, which led to development of targeted immune strategies to improve anti-
81 cancer T cell immunity in preclinical model systems and patients^{8, 9, 10}. Besides T_{reg} cells, also
82 regulatory myeloid cells were described, termed myeloid-derived-suppressor-cells (MDSCs)¹¹, -
83 that can be of monocytic (M-MDSCs) or polymorph nuclear (PMN-MDSCs) origin. Whereas
84 during acute inflammation monocytes, macrophages and granulocytes are found at sites of
85 inflammation and locally enhance T cell immunity, such as monocytes promoting local T cell
86 proliferation and immunity during acute liver inflammation¹², MDSCs typically arise in situations
87 of chronic inflammation in peripheral tissues including cancer^{13, 14, 15, 16}. Since discriminative
88 molecular markers for unequivocal identification of MDSCs do not yet exist, the molecular
89 mechanisms controlling T cell effector functions have been difficult to study. Here, we report on
90 the identification of a marker metabolite that identifies MDSCs and is causally involved in
91 metabolic suppression of T cell effector function.

92 Results

93 Dormant metabolic phenotype in MDSCs

94 Suppressive myeloid cells arise during chronic inflammation in tissues¹⁷, and tissue stromal cells
95 induce transition of monocytes into monocytic MDSCs¹⁶. We exploited this capacity of stromal
96 cells to convert human peripheral blood monocytes into MDSCs, which are phenotypically similar
97 to CD14⁺HLA-DR^{-/low} suppressive myeloid cells directly isolated from cancer patients¹⁶, to
98 characterize the mechanism of MDSC-mediated T cell suppression. Transcriptome analysis
99 showed less than 200 differentially expressed genes between MDSCs and monocytes, which did
100 not include surface molecules suitable for phenotypic discrimination or known immune
101 suppressive mediators to explain their suppressive activity (**supplementary table I-IV, Extended**
102 **Data Fig. 1**). Consistently, blockade of known immune suppressive mediators did not prevent
103 MDSC-mediated T cell suppression (**Extended Data Fig. 2**). Surprisingly, we found downregulation
104 of genes encoding glycolysis-related enzymes in MDSCs (**Fig. 1a, and Extended Data Table V**).
105 Indeed, MDSCs showed reduced glucose uptake and Glut1 surface expression (**Fig. 1b**), the main
106 transporter mediating glucose uptake in immune cells. As predicted from gene expression
107 analysis, hexokinase activity was lower in MDSCs (**Fig. 1c**). To validate these results, we isolated
108 CD14⁺HLA-DR^{-/lo} cells from tumor tissue of patients with hepatocellular carcinoma by enzymatic
109 digestion followed by density centrifugation and flow cytometric cell sorting. We confirmed
110 reduced glucose uptake and hexokinase activity in CD14⁺HLA-DR^{-/low} cells isolated from tumor
111 tissue of cancer patients (**Fig. 1d,e, and Extended Data Table VI**), which are considered to
112 represent MDSCs. Strikingly, MDSCs failed to utilize glucose for glycolysis and also showed
113 reduced cellular bioenergetics, i.e. lower mitochondrial membrane potential quantified by the
114 potentiometric mitochondrial dye DiIC₁(5) and lower baseline mitochondrial respiration revealed
115 by extracellular flux analysis (**Fig. 1f-h**). Together with reduced cellular ATP content (**Fig. 1i**) these
116 results revealed a rigorous reduction of cell metabolism to very low levels in viable MDSCs, and
117 raised the question as to whether this metabolic dormancy was involved in suppression of T
118 cells.
119

120 MDSCs paralyze CD8 T cell function

121 Signaling processes downstream of the TCR and the costimulatory receptor CD28 are important
122 for induction of glycolysis and glycolytic enzymes^{18, 19}. In particular hexokinase can also act as
123 protein kinase enhancing T cell activation²⁰. After contact with MDSCs, activation-induced
124 phosphorylation of key protein kinases downstream of the TCR was almost completely
125 prevented (**Fig. 2a** and **supplementary Fig. 3a-d**), indicating suppression of TCR signaling after
126 contact with MDSCs as compared to monocytes. T cell antigen receptor (TCR) and CD28 signaling
127 in CD8⁺ T cells act synergistically to increase glucose uptake and glycolysis²¹, which supports
128 execution of T cell effector function²². Co-culture of anti-CD3/28-activated CD8⁺ T cells with
129 MDSCs for 30 min fundamentally changed their metabolism. Such MDSC-exposed T cells failed to
130 increase glucose uptake, Glut-1 surface expression and hexokinase activity after activation, and
131 were similar to non-activated T cells (**Fig. 2b,c** and **Extended Data Fig. 4a-c**). In contrast, contact
132 with monocytes led to further increased glucose uptake and Glut-1 surface expression by
133 activated T cells (**Fig. 2b, c** and **Extended Data Fig. 4a-c**). Impaired glucose uptake into syngeneic
134 CD8⁺ T cells was also observed after co-culture with tumor-infiltrating CD14⁺HLA-DR^{-/lo} cells from
135 cancer patients (**Fig. 2d**), confirming the similarity between stromal cell-induced MDSCs and
136 MDSCs from cancer tissue. Furthermore, glycolysis and mitochondrial respiration were not
137 upregulated in T cells activated in presence of MDSCs as compared to monocytes (**Fig. 2e, f** and
138 **Extended Data Fig. 4d, e**). In consequence, ATP concentrations were reduced in T cells activated
139 in presence of MDSCs (**Fig. 2g** and **Extended Data Fig. 4f**). Strikingly, contact with MDSCs also
140 completely prevented cytokine expression (tumor necrosis factor (TNF) and interleukin- γ (IFN- γ))
141 and granzyme B release in T cells, and curtailed activation-induced proliferation of
142 CD45RA⁺CD62L^{hi} naïve, CD45RA⁺CX₃CR1⁺ effector, CD45RO⁺CD62L⁺ central memory or
143 CD45RO⁺CX₃CR1⁺ effector memory CD8⁺ T cells (**Fig. 2h, Extended Data Fig. 5a-g**). Importantly,
144 when activated CD8⁺ T cells were physically separated by transwell, MDSCs did not exert their
145 suppressive activity any more (**Fig. 2i**). These results suggested that MDSCs prevented T cell
146 activation by inhibiting signaling processes in a cell-contact dependent fashion, which
147 consecutively caused failure to upregulate metabolism and effector function.

148

149 These results led us to study MDSCs - T cell interaction further. We stained MDSCs or monocytes
150 with dyes that labeled mitochondria, endoplasmic reticulum, cytosolic proteins or plasma
151 membranes. We detected transfer of cytosolic constituents, either parts of labeled cellular
152 organelles or remaining cytosolic dye, into CD8⁺ T cells when located in direct vicinity (**Fig. 3a-c,**
153 **Extended Data Movies 1, 2**). Also labeled cytosolic constituents from tumor-infiltrating MDSCs
154 were transferred to T cells (**Fig. 3d**). In contrast, no or very little transfer of cytosolic constituents
155 was observed from human keratinocytes or fibroblasts to CD8⁺ T cells (**Fig. 3e**), consistent with
156 restriction of such transfer between immune cells^{23, 24}. Of note, also CD4⁺ T cells and natural
157 killer T (NKT) cells received cytosolic constituents from MDSCs (**Extended Data Fig. 6a**). No
158 transfer of surface molecules, however, was observed between MDSCs and T cells (**Fig. 3f**). To
159 demonstrate that such cell-cell transfer also occurred *in vivo*, we transferred mouse CD45.1⁺ OT-I
160 CD8⁺ T cells into tumor-bearing transgenic mice where myeloid cells expressed green fluorescent
161 protein (GFP) targeted to the mitochondrial matrix (*LysM-Cre x Rosa26-mitoGFP*). Transferred
162 CD8⁺ T cells, which were re-isolated from tumor tissue, were GFP^{pos} indicating cytosolic transfer
163 from myeloid to CD8⁺ T cells (**Extended Data Fig. 6c**). GFP^{pos}CD45.1⁺CD8⁺ T cells isolated from the
164 spleen, however, showed normal proliferation, whereas GFP^{pos}CD45.1⁺CD8⁺ T cells from tumor
165 tissue showed no proliferation after activation (**Extended Data Fig. 6d**), indicating that transfer of
166 GFP in different anatomic compartments by presumably different cells has a different effect on T
167 cell function – similar to the opposite effects of monocytes and MDSCs *in vitro* on the function of
168 T cells in their direct vicinity. We excluded transfer of entire organelles containing mitochondrial
169 DNA, because donor-specific single-nucleotide-polymorphisms in mitochondrial DNA from
170 MDSCs were not detected in acceptor CD8⁺ T cells (**Fig. 3g**). Together, these results revealed
171 transfer of cytosolic constituents rather than entire organelles from MDSCs into T cells in a cell-
172 contact dependent fashion.

173

174 **MDSCs paralyze CD8 T cells through the dicarbonyl methylglyoxal**

175 Given the importance of glycolysis for immune cell activation^{22, 25, 26}, we reasoned that blocking
176 of mitochondrial complex I activity through dimethylbiguanide (DMBG) or rotenone, which
177 increases glycolysis^{27, 28, 29, 30}, might revert the suppressive phenotype of MDSCs. However, only

178 DMBG-treatment of MDSCs reversed suppression of T cell proliferation (**Fig. 4a**) and re-installed
179 TCR signaling (data not shown), indicating a function of DMBG distinct from influencing
180 mitochondrial respiration. Guanidines also neutralize dicarbonyls that glycate molecules or
181 proteins with amino groups^{31, 32}, which led us to search for this class of reactive metabolites in
182 MDSCs. Strikingly, using highly sensitive detection of metabolites by ultrahigh performance liquid
183 chromatography data independent acquisition tandem mass spectrometry (UHLC-TOF-DIA-
184 MS/MS)³³ we identified methylglyoxal, a prototypic α -dicarbonyl³⁴, to be 30-fold enriched in
185 MDSCs (**Fig. 4b,c, supplementary table VII and supplementary Fig. 7a**). We confirmed
186 accumulation of methylglyoxal at the level of individual cells using the methylglyoxal-specific
187 fluorescent sensor methyl-diaminobenzene-BODIPY (MBo)³⁵. MDSCs showed higher MBo-
188 fluorescence compared with monocytes indicating presence of methylglyoxal (**Fig. 4d**).
189 Importantly, among myeloid CD14⁺ cells from cancer tissue we found MBo^{hi} cells that were HLA-
190 DR^{-/lo} (**Fig. 4e**), indicating that also patient-derived MDSCs had accumulated methylglyoxal.
191 Moreover, high MBo-fluorescence was found in both mouse CD11b⁺Ly6C⁺ and CD11b⁺Ly6G⁺ cells
192 isolated from tumor tissue or from the inflamed CNS tissue during the recovery phase of EAE
193 (**Fig. 4f**). Systematic analysis in different human immune cell populations revealed that high MBo-
194 fluorescence was selectively found in MDSCs and could therefore serve as molecular metabolic
195 marker (**Extended Data Fig. 7b**). When isolated from HCC patients MBo-fluorescence was only
196 detected in M-MDSCs but not in PMN-MDSCs (**Fig. 4g**), pointing towards differences between
197 human and murine PMN-MDSCs. Guanidines neutralize glycation activity of dicarbonyls^{36, 37}.
198 Strikingly, after incubation with DMBG but not molecules lacking guanidine-groups, human
199 MDSCs lost MBo-fluorescence and regained the capacity to take up glucose (**Fig. 4g,h, Extended**
200 **Data Fig. 7c**). Furthermore, DMBG also augmented aerobic glycolysis and mitochondrial
201 respiration in MDSCs up to the level observed in monocytes (**Fig. 4i,j**). We conclude from these
202 results that methylglyoxal not only serves as metabolic marker for MDSCs but that methylglyoxal
203 glycation activity, which is sensitive to DMBG neutralization, contributed to the dormant
204 metabolic phenotype of MDSCs and led us to characterize why methylglyoxal accumulated in
205 MDSCs.

206 Methylglyoxal can be generated by three distinct pathways (**Fig. 5a**), as byproduct of glycolysis
207 from glyceraldehyde 3-phosphate and dihydroxyacetone phosphate through spontaneous
208 dephosphorylation^{38, 39}, from acetol by acetone/actol mono-oxygenase (AMO; cytochrome
209 P4502E1)⁴⁰, or from aminoacetone by semicarbazide-sensitive amine oxidase (SSAO)^{38, 41}. We
210 performed competitive pulse-chase metabolic labeling experiments (50% ¹³C₆-glucose/50% ¹²C₆-
211 glucose), to discriminate between these pathways, i.e. methylglyoxal should contain three ¹³C-
212 atoms when derived from dihydroxyacetone phosphate^{38, 39}, two ¹³C-atoms when derived from
213 SSAO-activity and no ¹³C-atoms when derived from AMO-activity. A regular mass of 206 Da was
214 detected by UHPLC-TOF-DIA-MS/MS for 49% of 3-nitrophenylhydrazine-bound methylglyoxal
215 and 207 Da for 3%, reflecting the natural ¹³C-isotope distribution (**Fig. 5b**). However, 47% of
216 methylglyoxal detected in MDSCs had a mass of 208 Da (**Fig. 5b**), i.e. containing two ¹³C-atoms,
217 and indicated that methylglyoxal was generated by SSAO. This was corroborated by increased
218 expression of the *AOC3* gene that codes for SSAO (**Fig. 5c**). Intracellular methylglyoxal abundance
219 is regulated by glyoxalase and by glutathione, which neutralize dicarbonyls³⁶. Both, glyoxalase I
220 activity and cellular glutathione content were reduced in MDSCs compared to monocytes (**Fig.**
221 **5d,e**), indicating a dysbalance between generation and neutralization of methylglyoxal. SSAO-
222 inhibition with hydralazine or PXS-4618A prevented methylglyoxal accumulation in MDSCs and
223 reconstituted glucose uptake (**Fig. 5f,g**). These results prompted us to examine whether
224 methylglyoxal was involved in T cell suppression by MDSCs.

225 Within 10 min after contact with MDSCs but not monocytes, we detected methylglyoxal in CD8⁺
226 T cells, which was not observed when MDSCs were pretreated with DMBG (**Fig. 6a**). DMBG
227 treatment of MDSCs before co-culture also reconstituted CD8⁺ T cell uptake of glucose (**Fig. 6a**).
228 Furthermore, activation-induced cytokine production and granzyme B release were fully
229 functional in CD8⁺ T cells, when MDSCs or CD8⁺ T cells were pretreated with DMBG (**Fig. 6b**,
230 **Extended Data Fig. 8a-d**) demonstrating that DMBG abrogated the suppressive effect by acting in
231 MDSCs as well as in CD8⁺ T cells. In murine PMN-MDSCs, suppression of T cells was also
232 abolished by DMGB (**Extended Data Fig. 8d**). In contrast, DMBG did not show any effect on
233 suppression mediated by regulatory T cells (**Extended Data Fig. 8e**), which were also negative for
234 MBo-fluorescence. After separation from MDSCs, the suppression of T cells lasted for 3-4 h, and

235 DMBG shortened this time to 1 h until T cells started to take up glucose again (**Extended Data Fig.**
236 **8g,h**). In line with these findings, T cells co-cultured with MDSCs regained their capacity to
237 express cytokines upon activation at 4 h after re-isolation and separation from MDSCs (**Fig. 6b**).
238 This recovery phase was again shortened to 1 h by DMBG (**Fig.6b**). MDSC-mediated suppression
239 of T cell proliferation was overcome by DMBG or other guanidine-containing molecules (**Fig. 6c,**
240 **Extended Data Fig. 8a**). Of note, CD8⁺ T cell functions, which were augmented by co-culture with
241 monocytes, were not further increased by monocyte pretreatment with DMBG (**Fig. 6c, Extended**
242 **Data Fig. 8b**). Importantly, we did not observe increased apoptosis in T cells co-cultured with
243 MDSCs (**Extended Data Fig. 8i,j**), indicating that the suppressive activity of MDSCs did not kill but
244 rather stunned T cells.

245 Importantly, the suppression of T cell proliferation was strongest for MDSCs isolated from liver
246 cancer tissue and weaker when isolated from peritumoral liver tissue or peripheral blood,
247 isolated from the same patients with liver cancer, as shown by titrating numbers of MDSCs (**Fig.**
248 **6d**). DMBG reversed the suppressive effect of all M-MDSCs isolated from cancer, peritumoral
249 liver tissue and blood (**Fig. 6d**). Consistent with the lower suppressive capacity, M-MDSCs
250 isolated from blood showed weak to undetectable MBo-fluorescence effect (**see Fig. 4g**).
251 Nevertheless, DMBG-mediated reversal of T cell suppression indicated that methylglyoxal was
252 still present and functional, albeit at low levels was still present – albeit at low levels. It was not
253 possible to isolate PMN-MDSCs from tissue in sufficient quantities for suppression assays, but
254 tumor tissue-derived PMN-MDSCs did not show MBo-fluorescence and PMN-MDSCs isolated
255 from blood of tumor patients did not show suppressive activity (**Extended Data Fig. 8f**), which is
256 in line with findings from other groups^{42,43,44}.

257 Since methylglyoxal readily reacts with L-arginine, which is required for T cell activation^{45,46}, we
258 investigated whether the suppressive effect of MDSCs-transferred methylglyoxal was mediated
259 by depletion of amino acids, in particular L-arginine. To this end, we determined by mass
260 spectrometry the composition of free amino acids as well as advanced glycation end products
261 (AGPs) of amino acids and protein-bound amino acids in T cells. These experiments showed a
262 significant reduction in free L-arginine in T cells after co-culture with MDSCs but not monocytes
263 (**Fig. 6e,f**). Importantly, we also detected a simultaneous increase of the L-arginine-derived

264 reaction products with methylglyoxal, i.e. AGPs hydroimidazolone (MG-H1) and argpyrimidine
265 (**Fig 6e,f**). Furthermore, we detected a reduction of L-glutamine (**Fig. 6f**), which serves as a
266 precursor for glutathione that can scavenge methylglyoxal³⁴. There was no reduction in other
267 amino acids or AGPs in MDSC-exposed T cells (**Extended Data Fig. 9**) demonstrating a selective
268 depletion of amino acids that are critical for T cell activation. In summary, these data show that
269 contact with MDSCs led to depletion of L-arginine and concomitant increase in methylglyoxal-
270 derived glycation products of L-arginine in T cells, which may explain the methylglyoxal-mediated
271 paralysis of their effector functions.

272
273

274 **Methylglyoxal neutralization rescues anti-tumor immunity synergizing with checkpoint inhibition**

275 We employed the mechanistic understanding of MDSC-induced suppression of CD8⁺ T cell
276 effector function to increase efficacy of cancer immune therapy. Mouse melanoma cells
277 expressing ovalbumin (B16-OVA) were s.c. implanted into mice, followed ten days later by
278 therapeutic vaccination against ovalbumin to induce CD8⁺ T cell immunity against ovalbumin-
279 expressing cancer cells. Separate treatment with therapeutic vaccination, DMBG or checkpoint
280 inhibition with anti-PD-1 alone showed no or only marginal effects on tumor growth. The
281 combination of vaccination with DMBG showed a reduction in tumor growth (**Fig. 7a**). However,
282 strong and lasting tumor regression was observed when DMBG was combined with anti-PD-1
283 treatment independently from therapeutic vaccination. After 30 days, however, a relapse of
284 tumor growth was observed. Importantly, we found that tumor cells growing out after combined
285 DMBG/anti-PD-1 treatment had lost ovalbumin expression (**Fig. 7a, Extended Data Fig. 10 b**).
286 These results clearly demonstrated a synergistic effect of DMBG together with checkpoint
287 inhibition therapy using anti-PD1 to increase cancer-specific immune responses. Most likely,
288 DMBG reversed the suppressive effect of MDSCs on CD8⁺ T cells specific for immunogenic cancer
289 antigens, locally in tumor tissue, which might have increased the immune pressure on the tumor
290 and selection of tumor cells lacking ovalbumin expression.

291 These results prompted us to characterize CD8⁺ T cells and CD11b⁺ cells from tumor tissue and
292 spleen in detail. At day 17 after tumor inoculation, most CD11b⁺Ly6C⁺ and Ly6G⁺ cells isolated

293 from cancer tissue but not spleen showed MBo-fluorescence and were not capable of taking up
294 glucose (**Fig. 7b,c, Extended Data Fig. 10c,d,e**). In mice treated with DMBG, no MBo-fluorescence
295 was detected anymore in these cells and glucose uptake was rescued (**Fig. 7c,d**) independently of
296 vaccination or anti-PD-1 treatment. To directly investigate their suppressive function, we isolated
297 CD11b⁺Ly6C⁺ cells and incubated them *ex vivo* with CD8⁺ T cells. While CD11b⁺Ly6C⁺ cells from
298 cancer tissue irrespective of vaccination showed potent suppression of activation-induced T cell
299 proliferation, cells isolated from DMBG-treated mice did not suppress CD8⁺ T cell proliferation
300 anymore, while CD11b⁺Ly6C⁺ cells isolated from spleen always provided similar support for T cell
301 proliferation (**Fig. 7d, Extended Data Fig. 10f,g**). The numbers of effector CX₃CR1⁺ CD8⁺ T cells
302 found in cancer tissue increased after vaccination and were not further augmented by DMBG-
303 treatment, but these cells did not show MBo-fluorescence anymore and took up more glucose *ex*
304 *vivo* (**Fig. 7e**). Most importantly, numbers of CD8⁺ T cells isolated from cancer tissue, which
305 responded to antigen-specific restimulation *ex vivo* with robust cytokine expression, only
306 increased when mice received vaccination in combination with DMBG-treatment. While neither
307 MBo-fluorescence nor glucose uptake in monocytic cells in the tumor were influenced by anti-
308 PD-1 treatment alone, after combination with DMBG a significantly increased number of
309 antigen-specific cytokine-producing CD8⁺ T cells in the tumor was observed (**Fig. 7f-i, Extended**
310 **Data Fig. 10h,i**). Together, these results indicated that MDSCs paralyzed antigen-specific CD8⁺ T
311 cells in cancer tissues by a DMBG-sensitive mechanism that was mechanistically distinct from the
312 inhibitory effect through immune checkpoints and might explain the synergistic effect in
313 combination with checkpoint inhibition to increase cancer immune therapy.

314

315 Discussion

316 Here, we identify methylglyoxal as metabolic marker of MDSCs, which is responsible for the
317 dormant metabolic phenotype of MDSCs and for MDSC-mediated immune paralysis of CD8⁺ T
318 cells, and can serve as therapeutic target in combination with checkpoint inhibition to improve
319 immunotherapy against cancer.

320 MDSCs primarily inhibit effector functions of T cells and thereby impair immunity against
321 cancer⁴⁷. Many inhibitory mechanisms have been attributed to MDSC-mediated suppression of T

322 cell effector function, such as IL-10, TGF- β , arginase-1 to deplete extracellular L-arginine,
323 indoleamine 2,3-dioxygenase (IDO) and iNOS⁴⁸. However, the lack of a molecular marker to
324 unequivocally identify MDSCs made it difficult to assign to MDSCs the production of any of the
325 aforementioned regulatory molecules, which are often also produced by other immune
326 regulatory cell populations like regulatory T cells⁷. MDSCs are believed to be contained among
327 CD14⁺HLA-DR^{-/lo} cells⁴⁷. Using high-resolution mass-spectrometry, we have identified
328 methylglyoxal as marker metabolite for MDSCs that is generated from acetyl-CoA and glycine
329 through the enzyme SSAO. Detection with MBo revealed at the single-cell level that
330 methylglyoxal accumulated selectively in CD14⁺HLA-DR^{-/lo} cells isolated from human cancer
331 tissues but is not expressed by other immune cell populations, thus demonstrating the
332 usefulness of methylglyoxal to identify human MDSCs. The rapid acquisition of MBo-fluorescence
333 in T cells after 30 min of co-culture with MDSCs isolated from human cancer tissues further
334 suggested that methylglyoxal was readily transmitted from MDSCs to T cells.

335 Methylglyoxal belongs to the family of α -dicarbonyls, a group of molecules with glycation
336 capacity⁴⁹. Dicarbonyls attack amino/guanidine-groups (HN=C-(NH₂)-NH), thus targeting
337 preferentially the amino acids L-lysine and L-arginine as well as their residues in proteins to form
338 advanced glycation end-products that can render amino acids and proteins non-functional^{37, 50}.
339 The amino acid L-arginine is essential for T cell activation and execution of effector functions^{46, 51}
340 and the depletion of free L-arginine, as well as modifications of proteins containing L-arginine is
341 sufficient to block signaling and function of T cells^{52, 53, 54}.

342 Our results provide evidence that contact with MDSCs led to depletion of L-arginine within CD8⁺
343 T cells. At the same time, we detected methylglyoxal-derived glycation products of L-arginine
344 such as argpyrimidine and hydroimidazolone in T cells, which together suggests that MDSC-
345 derived methylglyoxal caused intracellular depletion of L-arginine in T cells and thereby induced
346 T cell paralysis. Methylglyoxal may suppress T cell function not only by chemical depletion of
347 cytosolic amino acids like L-arginine but also by rendering L-arginine-containing proteins through
348 glycation non-functional³⁷, such as protein kinases relevant for signal transduction or
349 mitochondrial proteins involved in mitochondrial respiration^{46, 55, 56, 57}. This intracellular
350 depletion of arginine by methylglyoxal is a highly efficient and rapid mechanism to deprive CD8⁺

351 T cells of their capacity to respond to activation signals and render them paralyzed, which is
352 mechanistically distinct from expression of arginase that consumes extracellular arginine to
353 deprive T cells of arginine sources⁴⁸.

354 Transfer of methylglyoxal from MDSCs to T cells required direct cell-cell contact, which may lead
355 to a more pronounced T cell suppression at sites where MDSCs accumulate, such as tumor
356 tissue. The identification of methylglyoxal as metabolic marker of MDSCs will allow to study
357 which cells of the tumor microenvironment may be involved in the induction of MDSCs. Our
358 observation that methylglyoxal-containing MDSCs were absent from secondary lymphoid tissues
359 points towards a predominant local effect of immune suppression by MDSCs within tumor tissue,
360 although MDSCs circulating in the blood may impair immune responses at distant sites from the
361 tumor.

362 Based on this mechanistic insight, we were able to neutralize the glycation function of
363 methylglyoxal with molecules containing amino/guanidine-groups or to prevent its formation by
364 inhibiting SSAO enzymatic activity. Both measures abrogated the ability of MDSCs to paralyze
365 CD8 T cells. Thus, methylglyoxal-mediated immune suppression by MDSCs is a promising
366 molecular target for immune intervention to increase CD8 T cell immunity against cancer.
367 Strikingly, we observed in a preclinical cancer model that neutralization of methylglyoxal with
368 DMBG had a strong synergistic effect with checkpoint inhibition to strengthen cancer-specific
369 CD8 T cell immunity. Since the combination treatment with DMBG/anti-PD1 did not increase
370 numbers but the functionality of effector CD8 T cells in tumor tissue, the discovery of
371 methylglyoxal as key immune suppressive mediator of intra-tumoral MDSCs opens new avenues
372 for targeted immune intervention in cancer patients.

373

374 **Acknowledgments**

375 We thank J. Schulze, M. Beyer and S. Schmitt (Life and Medical Science Institute, University of Bonn,
376 Germany) for isolating RNA and carrying out Illumina whole genome arrays; R. Weisskirchen (Institute of
377 Molecular Pathobiochemistry, Experimental Gene Therapy and Clinical Chemistry, RWTH University
378 Hospital Aachen, Germany) and J. Trebicka (Department of Internal Medicine I, University Clinic Bonn,
379 Germany) for the kind providing of LX2 cells; Raul Berger (Institute of Molecular Immunology and
380 Experimental Oncology, Technische Universität München, Munich, Germany) for performing Seahorse
381 experiments; C. Llanto, S. Michailidou and Silke Hegenbarth for their excellent technical support.

382 PK was supported by German Research Council (SFB TRR179) and German Center for Infection Research;
383 BH was supported by the German Cancer Aid; TK was supported by the German Research Council
384 (SFB1054, TR128, TR274, SyNergy (EXC 2145, ID 390857198)) and the ERC (CoG 647215).

385

386 **Competing interests' statement:** the authors declare to have no competing interests.

387

388 **Author contributions**

389 TB, AD, CS, SS, MH, KL, VL, UA, BLD, JS, LS, CF, NK, Tanja Bauer, ML, KE, SE, JEH, MA, MS, AH performed
390 experiments and analyzed data; SD, JS, UA performed bioinformatic analyses; performed NH, DH BS, DS,
391 FA, TM, HZ, MH, TK, CD, TH contributed specific technologies and reagents; BS, DS, TM, HS, MH, TK, CD,
392 TH PM, PK and BH designed experiments; PJM, PAK, BH wrote the manuscript, all authors read and
393 approved the manuscript.

394

395 **Figure legends**

396

397 **Legend to Figure 1: Adjustment of cell metabolism to very low levels in human MDSCs compared to monocytes. a,**
398 differentially expressed genes encoding glycolysis KEGG-pathway enzymes in monocytes (left) compared to stromal
399 cell-induced MDSCs (right; n = 3 independent biological samples). **b,** uptake of the glucose-analog 2-NBDG (n = 3)
400 and Glut-1 cell surface expression levels (3 experiments). **c,** hexokinase activity (n = 3 independent biological
401 samples). **d, e,** glucose uptake or hexokinase activity in CD14⁺HLA-DR⁺ (monocytes) or CD14⁺HLA-DR^{/low} cells
402 (MDSCs) from cancer patients (n =3 independent biological samples). **f,** extracellular acidification rate (ECAR) as
403 measure of aerobic glycolysis (n = 3). **g,** mitochondrial mass (Mitotracker green) and mitochondrial membrane
404 potential (DiIC₁(5)), GeoMean given in numbers (n = 3 independent biological samples). **h,** oxygen consumption rate
405 (OCR) as measure of mitochondrial respiration (n = 3 independent biological samples), statistical significance for
406 baseline OCR. **i,** total cellular ATP content (n = 3 independent biological samples). **p < 0.01; ***p < 0.001; two-way
407 unpaired t-test, diagrams plotted as SEM.

408

409 **Legend to Figure 2: MDSCs suppress activation-induced signaling and consequently glycolysis and effector functions in**

410 **CD8 T cells in a cell-contact dependent manner.** Activated human CD8⁺ T cells were co-cultured for 5 minutes (a), or
411 30 minutes (b and c, e-i) with MDSCs or monocytes (ratio 1:1), or human CD14⁺HLA-DR^{hi} monocytes or CD14⁺HLA-
412 DR^{/low} cells from cancer tissue (d). **a,** flow cytometric detection of activation-induced phosphorylation of signaling
413 molecules in CD8⁺ T cells co-cultured with MDSCs or monocytes at five minutes after anti-CD3/CD28 stimulation (n =
414 3 independent samples). **b,** fold change of surface Glut-1 expression and glucose uptake (n = 3 independent
415 samples). **c,** fold-change of hexokinase activity of FACSsorted CD8⁺ T cells (n =3 independent samples). **d,** glucose
416 uptake after co-culture with CD14⁺ cells from cancer tissue (n = 3 independent samples). **e,** time kinetics of glycolytic
417 rates. **f,** oxygen consumption rates (n = 3). **g,** fold change ATP levels (n = 3 independent samples) of FACSsorted
418 CD8⁺ T cells. **h,** IFN- γ , TNF expression of activated CD8⁺CD45RA⁺CX₃CR1⁺ T cells co-cultured with monocytes (red) or
419 MDSCs (blue) (n = 3). **i,** proliferation of CD8⁺ T cells in coculture with MDSCs or monocytes by CFSE- dilution or
420 separation in transwell (0.4 μ m pore size). Numbers indicate division indices. (n = 8 independent samples). *p < 0.05;
421 **p < 0.01; ***p < 0.001; two-way unpaired t-test; (F) ****p < 0.0001; two-way Anova, diagrams plotted as SEM.

422

423 **Legend to Figure 3: Transfer of cytosolic constituents from MDSCs to CD8 T cells. a,** Detection of MitoTracker Green

424 fluorescence in CD8⁺ T cells in co-culture (30 minutes) with MitoTracker Green-labeled MDSCs; transwell pore size
425 0.4 μ m, MDSCs lysis by hypo-osmotic shock (n = 3 independent biological samples; results shown gated for CD8 T
426 cells). **b,** transfer of cytosolic constituents from myeloid cells (Mitotracker) to CD8⁺ T cells (eF670) after coculture for
427 30 minutes; scale bar 10 μ m (n = 4 independent biological samples). **c,** quantification of transfer of cytosolic
428 constituents to CD8⁺ T cells by flow cytometry for monocytes (red) or MDSCs (blue) (n = 4 independent biological
429 samples). **d,** transfer of cytosolic constituents from tumor-infiltrating CD14⁺ cells of cancer patients, i.e. HLA-DR^{hi}
430 monocytes and HLA-DR^{/low} MDSCs labeled with MitoTracker, to CD8⁺ T cells in co-culture (30 minutes), results

431 shown gated for CD8⁺ T cells (n = 3 independent biological samples); most pronounced transfer into
432 CX₃CR1⁺CD45RO⁺ effector CD8⁺ T cells. **e**, no significant transfer of cytosolic constituents from MitoTracker-labeled
433 primary human fibroblasts or keratinocytes to CD8⁺ T cells in co-culture (30 minutes) (n = 3 independent biological
434 samples). **f**, no transfer of myeloid cell surface markers to CD8 T cells (n = 3 independent biological samples). **g**, no
435 detection of single nucleotide polymorphisms at position 152 of mitochondrial DNA from human MDSCs (donor) in
436 lysates of CD8⁺ T cells (acceptor). FACSsorted after co-culture (30 minutes) (n = 5 independent biological samples
437 separate donor acceptor experiments), demonstrating that no mitochondrial DNA was transferred from MDSCs to
438 CD8 T cells thus excluding transfer of entire DNA-containing mitochondria.

439
440 **Legend to Figure 4: Accumulation of dicarbonyl radical methylglyoxal is a metabolic marker for MDSCs and mediates**
441 **their dormant metabolic phenotype.** **a**, proliferation profiles of activated CD8⁺ T cells after co-culture with MDSCs
442 (blue) or MDSCs treated with rotenone (2 μM), or DMBG (200 μM) (purple) (n = 3). **b-j**, analyses of MDSCs. **b**,
443 volcano plot (p-value vs. log₂ fold-change) of 3-NPH-bound metabolites detected in MDSCs compared to monocytes
444 by UHPLC-TOF-DIA-MS/MS (red arrow indicates methylglyoxal, feature ID: 67, see supplementary Table VII) (n = 6
445 independent samples). **c**, ion chromatograms of 3-NPH-bound methylglyoxal (exact mass of 3-NPH-bound
446 methylglyoxal: 206.0579; tolerance: 0.01, n = 3). **d**, fluorescence intensity of the methylglyoxal-specific dye methyl-
447 diaminobenzene-BODIPY (MBo) in MDSCs and monocytes and **e**, in tumor-infiltrating CD14⁺ cells isolated from
448 cancer patients (n = 3). **f**, MBo-fluorescence intensity in murine CD11b⁺ cells from tumor tissue (B16-melanoma) or
449 from the central nervous system during the recovery phase (day 22 after immunization) of experimental
450 autoimmune encephalomyelitis (EAE) (n = 5). **g**, CD14⁺ or CD15⁺ cells were isolated from tumor tissue, liver tissue or
451 blood from the same patient and examined for the expression of methylglyoxal (n = 2). **h**, MBo-fluorescence
452 intensity in MDSCs after DMBG treatment (30 minutes) (n = 5). **i**, MBo-fluorescence and glucose-uptake in MDSCs
453 (30 minutes pretreatment with inhibitors), note absent effect by robenidine that does not contain a guanidine-
454 group (n = 3 independent samples). **j**, **k**, oxygen consumption and extracellular acidification rates of MDSCs (30
455 minutes DMBG pretreatment). OM = oligomycin, 2-DG = 2-deoxy-glucose, CCCP = carbonyl cyanide 3-chlorophenyl
456 hydrazine (n = 3 independent samples). ***p < 0.001; two-way unpaired t-test; (F) ****p < 0.0001; two-way Anova,
457 diagram plotted as SEM.

458
459 **Legend to Figure 5: Methylglyoxal accumulates in MDSCs in a semicarbazide-sensitive-amine oxidase (SSAO)**
460 **dependent fashion.** **b-e**, analyses of human MDSCs. **a**, schematic illustration of the different pathways for generation
461 of methylglyoxal in mammalian cells: spontaneous non-enzymatic dephosphorylation of glucose-derived dihydroxy-
462 acetonephosphate; acetone monooxygenase (AMO) mediated enzymatic generation from fatty acid-derived acetol;
463 SSAO mediated generation from glucose-derived and amino-acid-derived aminoacetone. **b**, metabolic pulse chase
464 (6hrs) with 50% ¹³C₆-glucose and UHPLC-TOF-DIA-MC/MS analysis of MDSC lysates showing relative abundance of
465 methylglyoxal isotopologues (technical triplicates, n = 2). **c**, AOC3 mRNA level (coding for SSAO) in MDSCs and

466 monocytes (n = 2 independent biological samples). **d**, glyoxalase I (Glo-I) activity (n=5 independent biological
467 samples). **e**, glutathione (GSH) quantification (n=5 independent biological samples). **f**, MBo-fluorescence intensity in
468 MDSCs generated in the presence of inhibitors (72 hours): the monoamine-oxidase A inhibitor clorgyline (100 nM),
469 the AMO inhibitor tetraethylthiuram-disulfid (TETD, 1 μ M), and SSAO-specific inhibitors hydralazine (15 μ M) and
470 PXS-4681A (500 nM). Incubation of MDSCs with inhibitors for 2 hours exclude direct neutralization of methylglyoxal.
471 DMBG used as a positive control that directly neutralizes glycation activity of methylglyoxal. (n = 4 independent
472 biological samples). **g**, glucose uptake by MDSCs in presence of the above-mentioned inhibitors with the short
473 incubation (2h) demonstrating that compounds did not have a direct effect on MDSCs. (n = 5). ns = not significant;
474 *p < 0.05; **p < 0.01; ***p < 0.001; two-way unpaired t-test, diagrams plotted as SEM.

475
476 **Legend to Figure 6: Guanidine-treatment of MDSCs abrogates their suppressive activity on CD8⁺ T cell effector**
477 **functions. a – f**, analysis of human activated CD8⁺ T cells in co-culture with MDSCs, that were pretreated (30
478 minutes) with indicated inhibitors. **a**, MBo-fluorescence in CD8⁺ T cells after 10 minutes of coculture with MDSCs or
479 monocytes (left) and glucose uptake (right) (n = 3 independent samples). **b**, intracellular cytokine staining of
480 activated CX₃CR1⁺CD45RO⁺ CD8⁺ T cells, (n = 3 independent samples). T cells were stimulated in the presence of
481 MDSCs (pretreated with DMBG, methylguanidine, aminoguanidine or rodenidine (200 μ M), where mentioned), T
482 cells were pretreated with DMBG, re-isolated after co-culture with MDSCs and stimulated after 1 or 4 hours, or
483 DMBG treated after directly or after 1 hour. **c**, proliferation of activated CD8⁺ T cells in co-culture with MDSCs or
484 monocytes in presence of indicated compounds (CFSE-dilution, numbers denote division indices) (n = 3). **d**, CD14⁺ or
485 CD15⁺ cells were isolated from tumor tissue, liver tissue or blood from the same patient were isolated and cocultured
486 with CFSE labeled, activated CD8⁺ T cells. Proliferation was measured by the dilution of CFSE (n = 2). **e, f**, free amino
487 acids and advanced glycation products were measured using SIDA-UHPLC-MS/MSMRM in CD8⁺ T cells after co-
488 culture with MDSCs or monocytes. **e**, ion chromatogram of free L-arginine in CD8⁺ T cells, **g**, quantification of amino
489 acids L-glutamine and L-arginine and glycation products argpyrimidine, MG-H1 and MOLD (n = 4). ns = not
490 significant; *p < 0.05; **p < 0.01; ***p < 0.001; two-way unpaired t-test, diagrams plotted as SEM.

491
492 **Legend to figure 7: DMBG treatment overcomes MDSC-induced suppression of CD8⁺ T cell function during therapeutic**
493 **anti-cancer vaccination. a-g**, at d10 after s.c. B16-OVA cancer cell inoculation, mice received ovalbumin adjuvanted
494 with CpG/ α GalCer, anti-PD-1 and/or DMBG in drinking water (40 mM), and analyses were performed at d17 (n = 5
495 mice). **a**, time kinetics of cancer growth in individual mice. **b, c**, MBo-fluorescence and glucose uptake of CD11b⁺
496 cells from cancer tissue and spleen. **d**, CD8⁺ T cell proliferation (CFSE-dilution) in co-culture with CD11b⁺Ly6C⁺ cells
497 or CD11b⁺Ly6G⁺ (FACSsorted) from cancer tissue or spleen (numbers denote division indices). **e - g**, MBo-
498 fluorescence and glucose uptake *ex vivo* in CD8⁺ T cells from tumor tissue or spleen. **h, i**, cytokine expression by CD8⁺
499 T cells from cancer tissue after *ex vivo* ovalbumin peptide-specific stimulation. ns = not significant; data are
500 presented as mean \pm SEM, *p < 0.05; **p < 0.01; ***p < 0.001; two-way unpaired t-test, diagrams plotted as SEM.

501

502 **References**

503

504 1. Spitzer, M.H. *et al.* Systemic Immunity Is Required for Effective Cancer Immunotherapy.
505 *Cell* **168**, 487-502 e415 (2017).

506

507 2. Williams, M.A. & Bevan, M.J. Effector and memory CTL differentiation. *Annual Rev*
508 *Immunol* **25**, 171-192 (2007).

509

510 3. Togashi, Y., Shitara, K. & Nishikawa, H. Regulatory T cells in cancer immunosuppression -
511 implications for anticancer therapy. *Nat Rev Clin Oncol* **16**, 356-371 (2019).

512

513 4. Veglia, F., Perego, M. & Gabrilovich, D. Myeloid-derived suppressor cells coming of age.
514 *Nat Immunol* **19**, 108-119 (2018).

515

516 5. Ribas, A. & Wolchok, J.D. Cancer immunotherapy using checkpoint blockade. *Science* **359**,
517 1350-1355 (2018).

518

519 6. Hori, S., Nomura, T. & Sakaguchi, S. Control of regulatory T cell development by the
520 transcription factor Foxp3. *Science* **299**, 1057-1061 (2003).

521

522 7. Bilate, A.M. & Lafaille, J.J. Induced CD4+Foxp3+ regulatory T cells in immune tolerance.
523 *Annu Rev Immunol* **30**, 733-758 (2012).

524

525 8. Sugiyama, D. *et al.* Anti-CCR4 mAb selectively depletes effector-type FoxP3+CD4+
526 regulatory T cells, evoking antitumor immune responses in humans. *Proc Natl Acad Sci U*
527 *S A* **110**, 17945-17950 (2013).

528

529 9. Bopp, T. *et al.* Cyclic adenosine monophosphate is a key component of regulatory T cell-
530 mediated suppression. *J Exp Med* **204**, 1303-1310 (2007).

531

532 10. Nishikawa, H. & Sakaguchi, S. Regulatory T cells in cancer immunotherapy. *Current*
533 *opinion in immunology* **27**, 1-7 (2014).

534

535 11. Bronte, V. *et al.* Recommendations for myeloid-derived suppressor cell nomenclature
536 and characterization standards. *Nat Commun* **7**, 12150 (2016).

537

538 12. Huang, L.R. *et al.* Intrahepatic myeloid-cell aggregates enable local proliferation of CD8(+)
539 T cells and successful immunotherapy against chronic viral liver infection. *Nat Immunol*
540 **14**, 574-583 (2013).

541

542 13. Pallett, L.J. *et al.* Metabolic regulation of hepatitis B immunopathology by myeloid-
543 derived suppressor cells. *Nat Med* **21**, 591-600 (2015).

544

- 545 14. Tcyganov, E., Mastio, J., Chen, E. & Gabrilovich, D.I. Plasticity of myeloid-derived
546 suppressor cells in cancer. *Curr Opin Immunol* **51**, 76-82 (2018).
547
- 548 15. Kumar, V. *et al.* Cancer-Associated Fibroblasts Neutralize the Anti-tumor Effect of CSF1
549 Receptor Blockade by Inducing PMN-MDSC Infiltration of Tumors. *Cancer cell* **32**, 654-668
550 e655 (2017).
551
- 552 16. Hochst, B. *et al.* Activated human hepatic stellate cells induce myeloid derived suppressor
553 cells from peripheral blood monocytes in a CD44-dependent fashion. *Journal of*
554 *hepatology* **59**, 528-535 (2013).
555
- 556 17. Ostrand-Rosenberg, S. & Fenselau, C. Myeloid-Derived Suppressor Cells: Immune-
557 Suppressive Cells That Impair Antitumor Immunity and Are Sculpted by Their
558 Environment. *J Immunol* **200**, 422-431 (2018).
559
- 560 18. Klein Geltink, R.I. *et al.* Mitochondrial Priming by CD28. *Cell* **171**, 385-397 e311 (2017).
561
- 562 19. Chang, C.H. *et al.* Posttranscriptional control of T cell effector function by aerobic
563 glycolysis. *Cell* **153**, 1239-1251 (2013).
564
- 565 20. Lu, Z. & Hunter, T. Metabolic Kinases Moonlighting as Protein Kinases. *Trends Biochem Sci*
566 **43**, 301-310 (2018).
567
- 568 21. Menk, A.V. *et al.* Early TCR Signaling Induces Rapid Aerobic Glycolysis Enabling Distinct
569 Acute T Cell Effector Functions. *Cell reports* **22**, 1509-1521 (2018).
570
- 571 22. Buck, M.D., Sowell, R.T., Kaech, S.M. & Pearce, E.L. Metabolic Instruction of Immunity.
572 *Cell* **169**, 570-586 (2017).
573
- 574 23. Onfelt, B., Nedvetzki, S., Yanagi, K. & Davis, D.M. Cutting edge: Membrane nanotubes
575 connect immune cells. *J Immunol* **173**, 1511-1513 (2004).
576
- 577 24. Watkins, S.C. & Salter, R.D. Functional connectivity between immune cells mediated by
578 tunneling nanotubules. *Immunity* **23**, 309-318 (2005).
579
- 580 25. O'Neill, L.A. & Pearce, E.J. Immunometabolism governs dendritic cell and macrophage
581 function. *J Exp Med* **213**, 15-23 (2016).
582
- 583 26. Ganeshan, K. & Chawla, A. Metabolic regulation of immune responses. *Annu Rev*
584 *Immunol* **32**, 609-634 (2014).
585
- 586 27. El-Mir, M.Y. *et al.* Dimethylbiguanide inhibits cell respiration via an indirect effect
587 targeted on the respiratory chain complex I. *J Biol Chem* **275**, 223-228 (2000).
588

- 589 28. Owen, M.R., Doran, E. & Halestrap, A.P. Evidence that metformin exerts its anti-diabetic
590 effects through inhibition of complex 1 of the mitochondrial respiratory chain. *Biochem J*
591 **348 Pt 3**, 607-614 (2000).
592
- 593 29. Wheaton, W.W. *et al.* Metformin inhibits mitochondrial complex I of cancer cells to
594 reduce tumorigenesis. *Elife* **3**, e02242 (2014).
595
- 596 30. Teeter, M.E., Baginsky, M.L. & Hatefi, Y. Ectopic inhibition of the complexes of the
597 electron transport system by rotenone, piericidin A, demerol and antimycin A. *Biochim*
598 *Biophys Acta* **172**, 331-333 (1969).
599
- 600 31. Kinsky, O.R. *et al.* Metformin Scavenges Methylglyoxal To Form a Novel Imidazolinone
601 Metabolite in Humans. *Chem Res Toxicol* **29**, 227-234 (2016).
602
- 603 32. Beisswenger, P. & Ruggiero-Lopez, D. Metformin inhibition of glycation processes.
604 *Diabetes Metab* **29**, 6S95-103 (2003).
605
- 606 33. Han, J., Gagnon, S., Eckle, T. & Borchers, C.H. Metabolomic analysis of key central carbon
607 metabolism carboxylic acids as their 3-nitrophenylhydrazones by UPLC/ESI-MS.
608 *Electrophoresis* **34**, 2891-2900 (2013).
609
- 610 34. Allaman, I., Belanger, M. & Magistretti, P.J. Methylglyoxal, the dark side of glycolysis.
611 *Front Neurosci* **9**, 23 (2015).
612
- 613 35. Wang, T., Douglass, E.F., Jr., Fitzgerald, K.J. & Spiegel, D.A. A "turn-on" fluorescent sensor
614 for methylglyoxal. *J Am Chem Soc* **135**, 12429-12433 (2013).
615
- 616 36. Rabbani, N. & Thornalley, P.J. The dicarbonyl proteome: proteins susceptible to
617 dicarbonyl glycation at functional sites in health, aging, and disease. *Ann N Y Acad Sci*
618 **1126**, 124-127 (2008).
619
- 620 37. Rabbani, N., Xue, M. & Thornalley, P.J. Methylglyoxal-induced dicarbonyl stress in aging
621 and disease: first steps towards glyoxalase 1-based treatments. *Clin Sci (Lond)* **130**, 1677-
622 1696 (2016).
623
- 624 38. Phillips, S.A. & Thornalley, P.J. The formation of methylglyoxal from triose phosphates.
625 Investigation using a specific assay for methylglyoxal. *Eur J Biochem* **212**, 101-105 (1993).
626
- 627 39. Ohmori, S., Mori, M., Shiraha, K. & Kawase, M. Biosynthesis and degradation of
628 methylglyoxal in animals. *Progress in clinical and biological research* **290**, 397-412 (1989).
629
- 630 40. Ray, S. & Ray, M. Formation of methylglyoxal from aminoacetone by amine oxidase from
631 goat plasma. *J Biol Chem* **258**, 3461-3462 (1983).
632

- 633 41. Lyles, G.A. & Chalmers, J. The metabolism of aminoacetone to methylglyoxal by
634 semicarbazide-sensitive amine oxidase in human umbilical artery. *Biochem Pharmacol* **43**,
635 1409-1414 (1992).
636
- 637 42. Mizukoshi, E. *et al.* Myeloid-derived suppressor cells correlate with patient outcomes in
638 hepatic arterial infusion chemotherapy for hepatocellular carcinoma. *Cancer Immunol*
639 *Immunother* **65**, 715-725 (2016).
640
- 641 43. Gao, X.H. *et al.* Circulating CD14(+) HLA-DR(-/low) myeloid-derived suppressor cells
642 predicted early recurrence of hepatocellular carcinoma after surgery. *Hepatol Res* **47**,
643 1061-1071 (2017).
644
- 645 44. Arihara, F. *et al.* Increase in CD14+HLA-DR -/low myeloid-derived suppressor cells in
646 hepatocellular carcinoma patients and its impact on prognosis. *Cancer Immunol*
647 *Immunother* **62**, 1421-1430 (2013).
648
- 649 45. Bronte, V., Serafini, P., Mazzoni, A., Segal, D.M. & Zanovello, P. L-arginine metabolism in
650 myeloid cells controls T-lymphocyte functions. *Trends Immunol* **24**, 302-306 (2003).
651
- 652 46. Geiger, R. *et al.* L-Arginine Modulates T Cell Metabolism and Enhances Survival and Anti-
653 tumor Activity. *Cell* **167**, 829-842 e813 (2016).
654
- 655 47. Gabrilovich, D.I., Ostrand-Rosenberg, S. & Bronte, V. Coordinated regulation of myeloid
656 cells by tumours. *Nat Rev Immunol* **12**, 253-268 (2012).
657
- 658 48. Gabrilovich, D.I. Myeloid-Derived Suppressor Cells. *Cancer Immunol Res* **5**, 3-8 (2017).
659
- 660 49. Rabbani, N. & Thornalley, P.J. Dicarbonyl stress in cell and tissue dysfunction contributing
661 to ageing and disease. *Biochem Biophys Res Commun* **458**, 221-226 (2015).
662
- 663 50. Nemet, I. & Varga-Defterdarovic, L. Methylglyoxal-derived beta-carbolines formed from
664 tryptophan and its derivatives in the Maillard reaction. *Amino Acids* **32**, 291-293 (2007).
665
- 666 51. Murray, P.J. Amino acid auxotrophy as a system of immunological control nodes. *Nat*
667 *Immunol* **17**, 132-139 (2016).
668
- 669 52. Chantranupong, L. *et al.* The CASTOR Proteins Are Arginine Sensors for the mTORC1
670 Pathway. *Cell* **165**, 153-164 (2016).
671
- 672 53. Saxton, R.A., Chantranupong, L., Knockenhauer, K.E., Schwartz, T.U. & Sabatini, D.M.
673 Mechanism of arginine sensing by CASTOR1 upstream of mTORC1. *Nature* **536**, 229-233
674 (2016).
675

- 676 54. Wang, S. *et al.* Metabolism. Lysosomal amino acid transporter SLC38A9 signals arginine
677 sufficiency to mTORC1. *Science* **347**, 188-194 (2015).
678
- 679 55. Cheng, C.T. *et al.* Arginine starvation kills tumor cells through aspartate exhaustion and
680 mitochondrial dysfunction. *Commun Biol* **1**, 178 (2018).
681
- 682 56. Taheri, F. *et al.* L-Arginine regulates the expression of the T-cell receptor zeta chain
683 (CD3zeta) in Jurkat cells. *Clin Cancer Res* **7**, 958s-965s (2001).
684
- 685 57. Qiu, F. *et al.* Arginine starvation impairs mitochondrial respiratory function in ASS1-
686 deficient breast cancer cells. *Sci Signal* **7**, ra31 (2014).
687

688 Methods

689 Animal models and therapeutic vaccination

690 All animal experiments were performed according to the federal German law regarding the
691 protection of animals (ROB-55.2-2532.Vet_02-193 & ROB-55.2-2532.Vet_02-17-234). C57Bl/6J
692 mice, H2-K^bSIINFEKL restricted TCR-transgenic animals (OT-I) and LysM-Cre/B6;129-
693 Gt(ROSA)26Sor^{tm4(CAG-EGFP)Nat}/JRosa-mitoGFP (Jackson stock: 004781⁶⁰; Jackson stock: 021429⁶¹)
694 were bred according to the FELASA guidelines. B16-OVA cells, obtained from A.-K. Heine,
695 Institute of Experimental Immunology, University of Bonn, were cultured in DMEM media
696 containing 10% FCS, 200 mg/ml penicillin, 200 U/ml streptomycin, 2 mM L-glutamine and 400
697 µg/ml G418. For tumor implantation, 5×10^5 B16 melanoma cells were injected subcutaneously
698 into the left flank. Tumor size was measured using digital caliper and tumor volume was
699 calculated using the ellipsoid formula $V = \frac{4}{3}\pi r^2$. After 10 days, mice were either vaccinated
700 using 200 µg ovalbumin with 20 µg CpG-oligonucleotide 1668 (TBI Mol) and 0.2 µg α-
701 galactosylceramide (Axxora) in 100 µl PBS. DMBG was administrated via drinking water (40 mM).
702 Anti-PD-1 (clone 29.F1A12) was applied i.p. every 3rd day (200 µg). Experimental autoimmune
703 encephalomyelitis was induced by subcutaneous application of 200 µg MOG(35-55) peptide
704 (MEVGWYRSPFSRVVHLYRNGK) and 500 µg *Mycobacterium tuberculosis* H37Ra in Freund's
705 adjuvant oil with additional intravenous injection of 200 ng pertussis toxin on day 0 and 2, as
706 previously described⁶².

707

708 Antibodies

709 The following antibodies were used experiments with human cells: anti-CD1c (L161), anti-CD3
710 (HIT3a), anti-CD4 (OKT4), anti-CD8 (SK1), anti-CD11c (3.9), anti-CD14 (63D3), anti-CD16 (3G8),
711 anti-CD19 (HIB19), anti-CD20 (2H7), anti-CD24 (ML5), anti-CD25 (BC96), anti-CD27 (M-T271),
712 anti-CD38 (HB-7), anti-CD40 (5C3), anti-CD45RA (HI100), anti-CD45RO (UCHL1), anti-CD56
713 (5.1H11), anti-CD62L (DREG-56), anti-CD95 (DX2), anti-CD123 (6H6), anti-CD127 (A019D5), anti-
714 CD158 (HP-MA4), anti-CD197 (G043H7), anti-CD274 (29E.2A3), anti-CD303 (201A), anti-CD314
715 (1D11) anti-IgM (MHM-88), anti-IgG (HP6017), anti-HLA-DR (L243), anti-TNF (Mab11), anti-IFN-γ
716 (4S.B3), anti-Granzyme b (GB11), anti-Glut-1 (polyclonal, Novus Biologicals), anti-CX3CR1 (2A9-

717 1), anti-phospho-Zap70 (n3kobu5), anti-phospho-LCK (SRRCHA), anti-phospho-AKT (SDRNR),
718 anti-phospho-mTOR (MRRBY), anti-phospho-ERK (MILAN8R). For mice, the following antibodies
719 were used: anti-CD3 (145-2C11), anti-CD4 (RM4-5), anti-CD8 (53-6.7), anti-CD11b (M1/70), anti-
720 CD11c (N418), anti-Ly6C (4K1.4), anti-Ly6G (1A8) anti-F4/80 (BM8), anti-I-A/I-E (M5/114.15.2),
721 anti-NK1.1 (PK136), anti-B7-H1 (10F.9G2), anti-IFN- γ (XM61.2), anti-TNF (MP6-XT22) anti-CD25
722 (PC61), anti-Foxp3 (FJK16S), anti-CD62L (MEL-14), anti-CD44 (IM7), anti-CD45.1 (A20), anti-
723 CD45.2 (104), anti-MerTK (2B10C42). If not otherwise specified, antibodies were from Sony
724 Biotechnology or BioLegend.

725

726 **Flow cytometry and FACS sorting**

727 The phenotype of immune cells was determined by multicolor flow cytometry using a Sony
728 SP6800 or Sony SA3800 spectral analyzer (both Sony Biotechnology). FACS-Sorting of cells was
729 done using a Sony SH800 cell sorter. Data were analyzed using FlowJo software 10.0.8 (TreeStar
730 Inc.)

731

732 **Immune cell isolation and culture**

733 All experiments with human blood or human liver samples were performed in accordance to the
734 ethic votes 434/17S, 564/18SAS and 232/19S. Informed written consent was obtained from each
735 patient. Peripheral blood mononuclear cells (PBMCs) were isolated from freshly drawn blood by
736 density gradient centrifugation. Splenic and tumor infiltrating cells in mice were isolated as
737 described previously⁵⁸. If not specified, chemicals and kits were purchased from ThermoFisher
738 Scientific or Sigma Aldrich. Briefly, immune cells were isolated from spleen and tumor tissues by
739 mechanical disruption and tumor tissue was further digested with 0.1% collagenase (Sigma-
740 Aldrich) in RPMI for 10 min at 37°C. Single cells were isolated using 40% percoll (GE Healthcare)
741 and Ficoll density gradient centrifugation. Monocytes and CD8⁺ T cells were further purified by
742 immunomagnetic separation using anti-CD8 or anti-CD11b microbeads and AutoMACS (Miltenyi
743 Biotech), followed by FACS-Sort gating on CD11b⁺Ly6C⁺ or CD11b⁺Ly6G⁺ cells.

744 Human tumor tissue was mechanically shredded followed by enzymatic digestion with 0.1%
745 collagenase and 0.1% DNase in RPMI at 37°C for 30 min. Single cells were isolated using 40%

746 percoll (GE Healthcare) and Ficoll density gradient centrifugation. Monocytes and CD8⁺ T cells
747 were further purified by immunomagnetic separation using anti-CD8 or anti-CD14 microbeads
748 and AutoMACS (Miltenyi Biotech). MDSCs and monocytes were isolated from peripheral blood
749 mononuclear cells by FACS-Sort gating on CD14⁺HLA-DR^{-/lo} or CD14⁺HLA-DR⁺ cells.

750

751 **Induction of human MDSCs from monocytes by stromal cells**

752 Human monocytes (10⁶) isolated from peripheral blood of healthy volunteers were cultured on a
753 confluent layer of human stromal liver cells, i.e. myofibroblast cells (LX2)⁵⁹ (4 × 10⁵ cells in 24-
754 well plates) in RPMI supplemented with penicillin (200 mg), streptomycin (200 U/ml), L-
755 glutamine (2 mM) and 10% FCS for three days without medium change. Viable MDSCs were
756 separated from myofibroblasts by FACS-Sorting before use in functional assays. MDSCs
757 generated from monocytes were characterized by downregulation of HLA-DR and their capacity
758 to inhibit proliferation of anti-CD3/CD28 activated CD8⁺ T cells. Where indicated, 100 nM (2,4-
759 dichlorophenoxy)-N-methyl-N-prop-2-ynylpropan-1-amine hydrochloride), 1 μM TETD,
760 (diethylcarbamothioylsulfanyl N, N-diethylcarbamodithioate), 15 μM phthalazine-1-ylhydrazine,
761 50 nM PXS-4681A ((E)-2(aminomethyl)-3-fluoroprop-2-enoxy)-benzenesulfonamide) or 200 μM
762 dimethylbiguanide (DMBG), methylguanidine, aminoguanidine, (4-Chlorophenyl)-5-
763 isopropylbiguanid or tolylbiguanide were added during the co-culture with stromal cells.

764

765 **T cell proliferation assay**

766 Isolated CD8⁺ T cells and CD14⁺ cells were co-cultured at a ratio 1:1 and T cells were activated
767 with anti-CD3/CD28 coated Dynabeads (1 μl/ 10⁶ cells; 4 × 10⁴ beads / 10⁶ cells). As indicated,
768 cells were labeled with carboxyfluorescein-succinimidyl-ester (CFSE) for quantitative
769 determination of proliferation or cells were incubated for 4 h with monensin/brefeldin A when
770 subjected to intracellular cytokine staining. Where indicated, cells were treated with L-NO-
771 hydroxyl-L-arginine (L-NOHA) (10 μM), L-NG-monomethyl-L-arginine (L-NMMA) (10 μM),
772 Mn(III)tetrakis(4-benzoic acid)porphyrin Chloride (MnTBAP) (40 μM), 1-MT (20 μM), anti-TGF-β
773 (1D11), anti-IL-10 (JES3-19F1), anti-PD-1 (EH12.2H7) (40 μg/ml each), retinoic acid (500 nM),
774 DMBG (200 μM), methylguanidine, aminoguanidine, (4-Chlorophenyl)-5-isopropylbiguanid or

775 tolylbiguanide (200 μ M) 3-bromopyruvate (60 μ M) or rotenone (2 μ M). Proliferation was
776 determined by dilution of CFSE and division/proliferation index were calculated using FlowJo
777 10.4.2.

778 **Measurement of specific analytes**

779 **Arginase assay.** Immune cells were isolated, washed twice with PBS and resuspended in 50 μ l
780 water containing 0.1% Triton-X and protease inhibitor mixture (Roche Molecular Diagnostics)
781 and incubated for 30 min at 37°C. 50 μ l Tris-HCl (pH 8; 25 mM) containing 333 μ M MnCl₂ was
782 added followed by heating up the mixture up to 56°C for 10 min. 100 μ l of L-Arginine solution
783 (0.5 M) (Sigma-Aldrich) was added and the samples were incubated at 37°C for 30 min. The
784 hydrolysis reaction was stopped by adding 10% H₂SO₄ and 25% H₃PO₄ in H₂O. 40 μ l α -
785 isonitrosopropiophenone was added, heated up to 96°C for 45 min. Urea concentration was
786 determined by absorbance at 540 nm using a Tecan Reader.

787

788 **NO-and ROS measurement.** NO was measured using the modified Griess reagent (Sigma) and
789 ROS production was measured by using 5 μ M 2,7-Dichlorofluorescein diacetate (H₂DCFDA)
790 according to the manufacturer's protocol.

791

792 **Cytokine measurement in supernatants.** Cytokine quantification was done using ELISA for IL-1 β ,
793 IL-6, IL-10 and TNF (all BioLegend) according to the manufacturer's protocol.

794

795 **Hexokinase colorimetric assay.** The activity of hexokinase in cellular lysates was analyzed by
796 measuring the NADH production per time in a colorimetric assay according to the
797 manufacturer's protocol.

798

799 **ATP assay.** The ATP level of cells was analyzed using the ATP Assay Kit according to the
800 manufacturer's protocol.

801

802 **Glucose uptake assay.** Cells were cultured in glucose-free RPMI and incubated with 10 μ M (2-N-
803 (7-Nitrobenz-2-oxa-1,3-diazol-4yl)-Amino)-2-Deoxyglucose (2-NBDG) for 30 min followed by
804 determination of 2-NBDG fluorescence intensity by flow cytometry.

805

806 **Glyoxalase assay.** The enzymatic activity of glyoxalase I was measured using the “Glyoxalase I
807 Activity Assay Kit” from Sigma and is based on the change of absorbance at 240 nm due to the
808 conversion of methylglyoxal (substrate) to S-lactoylglutathione in the presence of reduced
809 glutathione (co-substrate). Briefly, cell pellets were permeabilized in assay buffer supplemented
810 with 0.1% Triton-X for 5 min at 21°C in an UV-transparent 96-well plate. Assay buffer containing
811 substrate and co-substrate was added and the increase of absorbance at 240 nm within 20 min
812 was measured to calculate the enzymatic activity. The activity was normalized to the protein
813 concentration of the sample, as measured with a standard colorimetric protein assay (Bio-Rad,
814 Laboratories Inc.).

815

816 **Immunoblot**

817 CD8⁺ T cells were stimulated with CD3/CD28 antibodies and either left alone or co-cultured in
818 the presence of monocytes or MDSCs for different periods of time. Subsequently, cells were
819 lysed in buffer containing 1% lauryl maltoside (LM) (N-dodecyl β -maltoside), 1% NP-40, 1 mM
820 Na₃VO₄, 1 mM PMSF, 10 mM NaF, 10 mM EDTA, 50 mM Tris pH 7.5, and 150 mM NaCl for 20
821 min on ice. Lysates were centrifuged and supernatants were incubated at 99°C for 5 min in
822 sample buffer containing β -mercaptoethanol before SDS-PAGE. Proteins were transferred onto a
823 nitrocellulose membrane (Amersham) and blocked with TBS containing 5% milk for 1 h at 21°C
824 The following antibodies were used to detect phosphorylated proteins: phospho-Zap70 (Tyr319),
825 phospho-LAT (Tyr191), phospho-PLC- γ 1 (Tyr783), and phospho-Erk1/2 (Thr202/Tyr204) (all from
826 Cell Signaling). An anti- β -actin antibody (clone AC15) was used to show equal loading.
827 Membranes were subsequently incubated with HRP-labeled secondary antibodies for 1 h and
828 phosphorylated proteins were detected using the ECL system (Amersham).

829

830 **Bioenergetics measurements**

831 Immune cells were seeded on a Seahorse 96-well plate (10^5 cells/well) in unbuffered RPMI
832 medium, containing 10 mM glucose and 2 mM glutamine and additionally supplemented with 2
833 mM glutamine and manually adjusted to pH 7.4. For oxidative profiling, 2 μ M oligomycin to block
834 ATP synthesis, 1.5 μ M CCCP to uncouple mitochondria proton pumping and 2 μ M antimycin A
835 and rotenone each to block electron transport chain, were injected during measurement of
836 oxygen consumption rates (OCR) in a Seahorse XF 96 Analyzer (Agilent Technologies). For
837 glycolytic profiling, immune cells were seeded in unbuffered, glucose-free DMEM (Seahorse
838 Bioscience, Agilent Technologies), manually adjusted to pH 7.4. Glycolysis, monitored as
839 extracellular acidification rate (ECAR), was started after addition of 10 mM glucose, followed by
840 1 μ M oligomycin to block mitochondrial ATP synthesis and 20 mM deoxyglucose (DG) that
841 reduces ECAR to glycolysis-unrelated levels. Glycolytic reserve was calculated as difference of
842 ECAR after oligomycin injection and baseline ECAR. ATP-linked respiration states the difference
843 between OCR after oligomycin injection and baseline. LPS (100 ng/ml) and PMA (50 μ g/l) were
844 injected to monitor the glycolytic switch in T cells. If not specified chemicals and medium were
845 obtained from Merck, Sigma-Aldrich.

846

847 **ELISPOT for detection of Granzyme B secretion**

848 Granzyme B secretion was measured on 1×10^5 isolated T cells stimulated with 2 μ g/ml CEF
849 peptide pool (Cytomegalovirus (CMV), Epstein-Barr (EBV) and Influenza virus (Flu)) (Proimmune)
850 using the human Granzyme B ELISpot^{plus} Kit (Mabtech AB, NACKA Strand, Sweden) according to
851 the manufacturer's instructions. ELISpot plates were evaluated within three days after assay
852 performance using an automated reader system (CTL-ImmunoSpot[®] S6 Ultra-V Analyzer/CTL
853 ImmunoSpot 5.4 Professional DC Software, CTL Europe). Scanning and counting of ELISpot plates
854 was performed with automatically adjusted settings conducted by the reader. All obtained
855 counts were reviewed and certified by a second person during a quality control process.

856

857 **Mitochondrial staining**

858 Cells were stained using 200 nM Benzoxazolium,2-[3-[5,6-dichloro-1,3-bis[[4-
859 (chloromethyl)phenyl]methyl]-1,3-dihydro-2H-benzimidazol-2-ylidene]-1-propenyl]-3-methyl-

860 chloride (Mitotracker-Green) or 50 nM Mito-Probe 3H-Indolium, 2-(5-(1,3-dihydro-1,3,3-
861 trimethyl-2H-indol-2-ylidene)-1,3-pentadienyl)-1,3,3-trimethyl-iodide 36536-22-8 (D1CL1(5))
862 according to the manufacturer's protocol.

863

864 **Methylglyoxal detection at single cell level by flow cytometry**

865 The fluorescent sensor methyl diaminobenzene-BIODIPY (MBo), that specifically detects
866 methylglyoxal³⁵, was used to detect presence of methylglyoxal at the level of single cells using
867 flow cytometry. Cells were loaded with MBo (10 μM) for 30 minutes in RPMI (supplemented
868 with 10% FCS, 200 mg penicillin, 200 U/ml streptomycin and 2 mM L-glutamine) at 37°C, washed
869 and subjected to further cell surface antibody staining before flow cytometric evaluation.

870

871 **RNA isolation and quantitative PCR**

872 RNA was isolated using RNeasy Kit (Qiagen) and complementary DNA synthesis was done with
873 Superscript Velo (ThermoFisher) according to the manufacturer's instructions. Quantitative PCR
874 was performed with SYBR-Green (Roche Molecular Diagnostics) using the following primers:
875 *CYPA* forward: 5'-ATGCTCAACCCACCGTGT-3'; *CYPA* reverse: 5'-TCTGCTGTCTTTGGGACCTTGTC-
876 3', *TGFB* forward: 5'-gtggaaaccacaacgaaat-3'; *TGFB* reverse: 5'-CACGTGCTGCTCCACTTTTA-3',
877 *IDO1* forward: 5'-AGAGTCAAATCCCTCAGTCC-3'; *IDO1* reverse: 5'-AAATCAGTGCCTCCAGTTCC-3';
878 *AOC3* forward: 5'-GGAACCAAGTGTCAGAGCACA-3'; *AOC3* reverse: 5'-
879 GGACAAAGACCATATCCTCGGC-3'; *SERPINB14* forward: 5'-TGTTGGTGTGTTGCCTGATG-3';
880 *SERPINB14* reverse: 5'-TTGTTGCGATGTGCTTGATAC-3'. Samples were analyzed in triplicates
881 and normalized to endogenous *CYPA* mRNA abundance.

882 **Gene expression profiling of monocytes and MDSCs and bioinformatic analysis**

883 After 18 h of co-culture of human monocytes with stromal cells, myeloid cells were separated
884 from stellate cells by FACS sorting. RNA was isolated from 5×10^6 cells using TRIzol according to
885 the manufacturer's protocol. Biotin-labeled cRNA was generated using the TargetAmp Nano-g
886 Biotin-cRNA labeling Kit (Epicentre). Biotin labeled cRNA was generated using the TargetAmp
887 Nano-g Biotin-cRNA Labeling Kit for the Illumina System (Epicentre). cRNA was hybridized onto

888 Illumina HumanRef-12 (version 3) bead array that probed for 48,794 genes. The raw intensity
889 values were analyzed using Genome Studio. The probe intensities from Illumina HumanRef-12
890 gene chip were imported into the R environment (<http://www.r-project.org/>). The probes were
891 normalized using robust spline normalization (RSN) method in lumi-R-package⁶³. The
892 differentially expressed genes (DEGs) were identified using the Bioconductor package Limma⁶⁴.
893 We considered a particular gene as a DEG when its expression log₂ fold change 0.6 (absolute fold
894 change 1.5, corrected p-value (q-value) ≤ 0.05). Pathway enrichment analysis of DEGs was
895 performed using METASCAPE (accessed on 13/06/16, <http://metascape.org>)⁶⁵. Cell surface
896 proteome analysis was performed by comparing differently expressed genes in MDSCs with the
897 human cell surface proteome database (<http://wlab.ethz.ch/cspa>)⁶⁶.

898

899 **Mitochondrial DNA detection**

900 CD8⁺ T cells (“acceptor”) or monocytes (“donor”) were purified from the blood of two non-
901 related, healthy individuals. After 30 min of co-culture, viable CD8⁺ T cells were separated using a
902 SH800 cell sorter (Sony (Sony Biotechnology) in ultra-purity mode and whole DNA was isolated.
903 mtDNA was amplified via XL-PCR (single amplicon 16569 bp) and sequenced with an Illumina
904 MiSeq (Illumina Inc.). Donor specific homoplasmic single nucleotide polymorphism (SNP) were
905 identified and used to test for trans-cellular mtDNA transfer from donor to acceptor cells. To
906 control for contamination with donor cells due to false-sorting, donor-specific microsatellites of
907 nuclear DNA were analyzed. No contamination was detected, the limit of detection was
908 approximately 2%.

909

910 **Confocal live cell microscopy**

911 For live cell imaging, a PerkinElmer UltraVIEW VoX spinning disc microscope with Nikon TiE
912 equipped with the Hamamatsu EM-CCD ImagEM X2 camera, APO TIRF 60x NA1.49 oil immersion
913 objective and environment control system (37°C and 5% CO₂), was used. T cells were stained
914 with eF670 (1 μM) and monocytes with Mitotracker green (200 nM) for 15 min and placed in 8-
915 well glass bottom chambered slides (Ibidi) in imaging medium (RPMI). Chambered slides were
916 placed on the microscope and focus was “locked-in” using hardware-based autofocusing system.

917 Then, monocytes were added to the chambers and time-lapse acquisition started. The entire 3D
918 volume of cells was acquired by optical sectioning using piezo z-drive step of 0.5 μm (15 steps)
919 every 75 sec for a total imaging duration between 40-60 min. eF670 and Mitotracker green were
920 imaged using 640 nm laser with 705/90 filter and 488 nm laser with 525/50 filter, respectively.
921 Transmission (DIC) images were acquired in addition.

922 For ultra-structural analysis during live cell imaging, LSM 880 Airyscan and Airyscan FAST,
923 respectively, equipped with a Plan-Apochromat 63x NA1.2 water immersion objective was used
924 (Carl Zeiss Microscopy GmbH). T cells and monocytes were isolated. Monocytes were stained
925 with Mitotracker green (200 nM) and placed in 8-well glass bottom chambered slides (Ibidi) in
926 the imaging medium (RPMI). Then, monocytes were added to the chambers and time-lapse
927 acquisition started. The entire 3D volume of cells was acquired by optical sectioning using piezo
928 z-drive step of 0.173 μm (45 steps, total range of 7.6 μm) every 53 sec for a total imaging
929 duration of 1 h 28 min. Cells were imaged including nuclear staining, laser-DIC and MitoTracker
930 green using 405 nm, 488 nm and 633 nm lasers with emission bands of 420-480 nm (nuclear
931 stain) and 495-550 nm (MitoTracker green), respectively. Laser-DIC was added in an additional
932 track at 633 nm laser for optimized penetration depth at minimal bleaching. Images were
933 acquired at two-fold optical zoom resulting in 67.5 \times 67.5 μm^2 at a pixel size of 0.04 \times 0.04 μm^2 .

934

935 UHPLC-TOF-DIA-MS/MS analysis

936 Monocytes and MDSCs were isolated or induced as described above. For ^{13}C -labeling experiments,
937 medium containing 50% $^{13}\text{C}_6$ -Glucose (Merck) was used during induction of MDSCs.

938 Isolated cells were transferred into CK14 – 0.5 mL bead beater tubes (Bertin Technologies)
939 containing 1.4 mm diameter ceramic (zirconium oxide) beads. After addition of
940 acetonitrile/water (250 μL , 50/50, v/v), the samples were homogenized for 3 \times 30 sec with 20 s
941 breaks between at 7,800 rpm (Precellys Evolution Homogenizer, Bertin Technologies); to prevent
942 excessive heating during homogenization, samples were cooled with liquid nitrogen using a
943 Cryolys cooling system (Bertin Technologies). Subsequently, samples were equilibrated for 15
944 min at 21°C and centrifuged at 16,100 g and 4°C for 5 min (Centrifuge 5415 R, Eppendorf) and
945 the clear supernatant was stored at -80°C until further analysis. For derivatization, 40 μL of the

946 cell extract were mixed with 20 μ l of a solution of 3-nitrophenyl hydrazine (200 mM, 50:50, v/v,
947 ACN/H₂O) and 20 μ l of a 120 mM solution of N-(3-Dimethylaminopropyl)-N'-ethylcarbodiimide in
948 6 % pyridine (50:50, v/v, ACN/H₂O) and reacted for 30 min at 40 °C. Afterwards the mixture was
949 diluted with ACN/ H₂O (200 μ l, 50:50, v/v) and used directly for UHLC hyphenated with time-of
950 flight (TOF) mass spectrometry (MS) and fragment spectra were acquired by means of data
951 independent acquisition (DIA). For the analysis, an Nexera X2 UHPLC system (Shimadzu)
952 consisting of two LC-30AD pumps, a SIL-30AC auto sampler, a CTO-30A column oven and a CBM-
953 20A system controller was connected to 6600 TripleTof instrument (Sciex) equipped with an
954 IonDrive ion source (Sciex) operating in negative electrospray mode. After each fifth sample the
955 instruments calibration was verified and corrected using ESI Negative Calibration solution (Sciex)
956 and a Calibrant Delivery System (Sciex). UHPLC separation was performed on a Kinetex Phenyl-
957 Hexyl column (100 mm x 2.1 mm, 1.7 μ m Phenomenex) using water (mobile phase A) and
958 acetonitrile (mobile phase B) with 0.1% formic acid each and the following gradient program: 0
959 min 36% B, 2 min 36% B, 3.5 min 80% B, 5 min 100% B, 7 min 100% B, 8 min 36% B, 12 min 36%
960 B. The total flow of the chromatography was set to 0.25 mL/min and separation was performed
961 at 40°C. The mass spectrometer was operated in the SWATH mode with a series of 19
962 consecutive experiments per 1.05 sec measurement cycle. After starting with a high-resolution
963 scan of the intact precursor ions from 50 to 1000 m/z for 100 ms, fragment ions were generated
964 by means of collision-induced fragmentation subsequently for precursor ions within 18 separate
965 windows ranging from 50 to 600 m/z (window width 30 Da each, 1 Da overlap), the resulting
966 fragment spectra were recorded in the high sensitivity mode (50 ms acquisition per window). Ion
967 spray voltage was set at -4500 V and the following source parameters were applied: curtain gas
968 35 psi, gas 1 55 psi, gas 2 65 psi, temperature 500°C. Declustering potential was set to 80 V for
969 all experiments while the collision energy was 10 V for precursor ion scans and 35 V including 25
970 V collision energy spread for the fragmentation in the individual SWATH windows. The following
971 compounds, have been measured as references: 3-phosphoglycerat, fructose-6-phosphate,
972 fructose-1,6- diphosphate, glucose, glucose-6-phosphate, glutathione, glyoxal, lactate,
973 lactoylglutathione, methylglyoxal, nucleotide mix, organic acid mix, phosphoenolpyruvate,
974 pyruvate.

975
976 **Quantification of amino acids (AAs) and advanced glycation products (AGPs) by stable isotope**
977 **dilution analysis (SIDA-UHPLC-MS/MS).**

978 Amino acids (AAs) L-arginine (**1**), L-glutamine (**2**), L-methionine (**3**), L-asparagine (**4**), L-glutamic
979 acid (**5**), L-tyrosine (**6**), L-isoleucine (**7**), L-phenylalanine (**8**), L-lysine (**9**), L-serine (**10**), L-leucine
980 (**11**), L-tryptophan (**12**), L-aspartic acid (**13**) and L-alanine (**14**) as well advanced glycytion
981 products (AGPs) argpyrimidine (**15**), MG-H1 (**16**), imidazolysine (**17**), pyrraline (**18**),
982 carboxyethyllysine (**19**) and carboxymethyllysine (**20**) were analysed by means of two newly
983 developed SIDA-UHPLC-MS/MS_{MRM} methods separately. To this end, corresponding stable
984 isotope labelled AA standards L-arginine (¹³C₆-**1**), L-glutamine (¹³C₅-**2**), L-methionine (methyl-d₃-
985 **3**), L-asparagine (¹⁵N₂-**4**), L-glutamic acid (¹³C₅-¹⁵N-**5**), L-tyrosine (ring-d₄-**6**), L-isoleucine (¹³C₆-**7**),
986 L-phenylalanine (ring-d₅-**8**), L-lysine (¹³C₆-**9**), L-serine (¹³C₃-**10**), L-leucine (¹³C₂-**11**), L-tryptophan
987 (indole-d₅-**12**), L-aspartic acid (¹³C₄-¹⁵N-**13**) and L-alanine (¹³C₃-**14**) as well imidazolysine-¹⁵N₂ (**17**-
988 ¹⁵N₂), MG-H1-d₃ (**16**-d₃) for AGP analysis were utilized. AGPs were obtained from Iris-Biotech.
989 Stable isotope labelled AAs were bought from Cambridge Isotopes. Solvents used for LC-MS/MS
990 analysis were of LC-MS grade (Honeywell). Ultrapure water for UHPLC separation and mass
991 spectrometry was purified by means of a Milli-Q water advantage A 10 water system (Millipore).
992 Millipore-grade water was used for all experiments unless stated otherwise.

993
994 *Internal Standard (IS)*

995 Internal standards were prepared in stock solutions (500 μL) with concentrations given in
996 supplementary Table VIII and were prepared in ACN/H₂O (10/90, v/v). Imidazolysine-¹⁵N₂ (12.06
997 mmol/L, **17**-¹⁵N₂) and MG-H1-d₃ (13.1 mmol/L, **16**-d₃) were dissolved in D₂O and their exact
998 concentration was verified by means of quantitative NMR (qNMR) and it was stored at -20 °C
999 until used. Internal standard solutions for amino acid (AA) and advanced glycation product (AGP)
1000 analysis were prepared by diluting stock solutions 1:5 and 1:20 with ACN/H₂O (50/50, v/v),
1001 respectively.

1002
1003 *Sample preparation*

1004 Cells were lysed at 0°C by bead beater (Precellys Evolution Homogenizer, Bertin) at 7000 rpm for
1005 6 × 20 sec with 30 sec pause in between. Afterwards lysed cells were ultrafiltrated (Amicon Ultra,
1006 Merck, 3 kDa centrifugal filters; 13,600 × g, 30 min, 4 °C). Filtrates were dried by vacuum
1007 centrifugation (Eppendorf Concentrator Plus, 6 h, 30°C), solved in 100 µL H₂O, internal standard
1008 solutions (each 2 µL) were added and subjected to the UHPLC-MS/MS system. Recovered protein
1009 was eluted by centrifugation (1,000 × g, 5 min, 4 °C). According to Ahmed, Argirov⁶⁷ and
1010 Salomón, Sibbersen⁶⁸ hydrolysis was carried out with slight modifications. Protein samples were
1011 mixed with HCl (aq, 40 mM, 50 µL), thymol solution (1 mg/mL in 40 mM HCl, 10 µL) and pepsin
1012 solution (1 mg/mL in 40 mM HCl, 10 µL) and incubated at 37°C for 24 h in an Eppendorf
1013 Thermomixer at 400 rpm. Subsequently, each sample was buffered and neutralized by addition
1014 of sodium phosphate buffer (aq., 500 mM, 50 µL) and sodium hydroxide (aq., 260 mM, 9 µL).
1015 Further hydrolysis was conducted by Pronase E (1 mg/mL in 10 mM sodium phosphate buffer, 10
1016 µL) for 24 h at 37°C in an Eppendorf Thermomixer at 400 rpm. In the last hydrolysis step, leucine
1017 aminopeptidase and prolidase (each 1 mg/mL in 10 mM sodium phosphate buffer, 10 µL) were
1018 added and incubation was continued at 37 °C for 48 h using an Eppendorf Thermomixer at 400
1019 rpm. To each hydrolysate internal standards of AA and AGP were added (3 µL). Afterwards,
1020 samples were ultrafiltered (Amicon Ultra, 3 kDa centrifugal filters; 13,600 × g, 30 min, 4 °C),
1021 dried by vacuum centrifugation and reconstituted to a defined volume (150 µL) by addition of
1022 H₂O for UHPLC-MS/MS analysis.

1023

1024 *Ultra High Performance Liquid Chromatography-Mass Spectrometry (UHPLC-MS/MS)*

1025 LC-MS/MS analysis was conducted on a QTRAP 6500+ LC-MS/MS system connected to a ExionLC
1026 AD (Sciex) operated in the positive ESI mode (ion spray voltage, 5500 V): curtain gas, 35 V;
1027 temperature, 450 °C (AAs) or 500 °C (AGPs); gas 1, 55 psi; gas 2, 65 psi; collision-activated
1028 dissociation, 2 V; and entrance potential, 10 V. For compound optimization flow injection with a
1029 syringe pump (10 µL/min) and compound solutions in ACN (0.1% FA) were used.

1030 AAs and AGPs were separated on a BEH Amide column (100 × 2.1 mm, 1.7 µm, Waters).
1031 Chromatography was performed using an injection volume of 1 µL (AAs) or 2 µL (AGPs), a flow
1032 rate of 0.4 mL/min and a column temperature of 40°C. The solvent system consisted of A: 5 mM

1033 NH₄Ac and 0.1% formic acid in water and B: 5 mM NH₄Ac and 0.1% formic acid in
1034 acetonitrile/water (95/5, v/v). For AA and AGP analysis two separate methods were used sharing
1035 following gradient: 0 min, 90% B; 5 min, 85% B; 8 min, 70% B; 9 min, 0% B; 11 min, 0% B; 12 min,
1036 90% A; 14 min, 90% B. Data acquisition and instrumental control was performed using Analyst
1037 1.6.3 software (Sciex). AAs and AGPs were analysed in the positive multiple reaction monitoring
1038 (MRM) mode following MS/MS parameters as depicted in Table VIII.

1039

1040 *Calibration Curve and Linear Range.*

1041 For AGP analysis stock solutions of standards were prepared in D₂O and each concentration was
1042 verified by means of quantitative NMR (qNMR). Thereafter, a mixture of analytes with
1043 concentrations of 132.5 µmol/L (**15**), 750 µmol/L (**16**), 300.5 µmol/L (**17**), 215.5 µmol/L (**18**),
1044 214.5 µmol/L (**19**) and 118.5 µmol/L (**20**) were prepared and subsequently diluted by factors of
1045 2, 5, 10, 20, 50, 100, 200, 500, 1000, 2000, 5000, 10000, 20000, 50000 and 100000. Afterwards,
1046 diluted analyte mixtures were mixed with constant concentrations of IS MG-H1-d₃ (**16-d₃**, 0.655
1047 mmol/L) and imidazolysine-¹⁵N₂ (**17-¹⁵N₂**, 0.606 mmol/L). Triplicate UHPLC-MS/MS analysis
1048 calibration curves were prepared by plotting peak area ratios of argpyrimidine (**15**), MG-H1 (**16**),
1049 pyrrolidine (**18**), carboxyethyllysine (**19**) and carboxymethyllysine (**20**) to the internal standard MG-
1050 H1-d₃ (**16-d₃**) against concentration ratios of the analytes to the IS using linear regression.
1051 Calibration curve of imidazolysine (**17**) was created by plotting peak ratios to the internal
1052 standard imidazolysine-¹⁵N₂ (**17-¹⁵N₂**) against concentration ratios of respective analyte and
1053 internal standard.

1054 AA analysis was conducted first by dilution (1:10, 1:20, 1:50, 1:100, 1:200, 1:500, 1:1000, 1:2000,
1055 1:5000 and 1:10000) of an AA mix with concentrations referred to Table IX. Subsequently, to
1056 each diluted AA standard solution diluted IS (1/20 dilution of stock solution) was added to a
1057 dilution factor of 250 referred to IS concentrations in Table IX. Calibration curves were created
1058 by triplicate UHPLC-MS/MS measurements and plotting peak area ratios AAs to corresponding
1059 internal standards by using a linear regression model.

1060 The response was linear for each analyte (AAs and AGPs) with correlation coefficients of >0.99
1061 for chosen molar ratios and the contents of AGPs in the samples were calculated using the

1062 respective calibration function. Determination of the limit of detection (LOD) at a signal-to-noise
1063 ratio of 3 and the limit of quantitation (LOQ) at a signal-to-noise ratio of 10 revealed the
1064 following values: LOD: $\leq 0.0001 \mu\text{M}$; LOQ $\leq 0.0005 \mu\text{M}$.

1065

1066 **Nuclear Magnetic Resonance Spectroscopy (NMR)**

1067 One-dimensional ^1H quantitative NMR (qNMR) experiments were acquired on a 400 MHz Avance
1068 III spectrometer equipped with a Double Resonance Broadband probe (Bruker as reported by ⁶⁹.
1069 Chemical shifts are reported in parts per million, relative to solvent signal of D_2O (7.26 ppm). All
1070 pulse sequences were taken from Bruker software library. For data processing Topspin NMR
1071 software (version 3.2; Bruker) was used.

1072

1073 **Statistical analysis**

1074 Statistical analyses were performed with Graph-Pad Prism 6 (GraphPad Software, Differences
1075 between groups were calculated by Student's two-way unpaired t-test, two-way ANOVA or
1076 Mantel-Cox-test. Statistical significance is depicted as *P*-value ($P^* < 0.05$; $P^{**} < 0.01$; $P^{***} < 0.001$;
1077 $P^{****} < 0.00001$).

1078

1079 **Data availability**

1080 The microarray data generated from human MDSCs compared to monocytes were deposited at:
1081 <https://www.ncbi.nlm.nih.gov/geo/query/acc.cgi?acc=GSE131679>. The data that support the
1082 findings of this study are available from the corresponding authors upon request.

1083 Further information can be found in the Life Sciences Reporting Summary.

1084 References

1085
1086
1087
1088
1089
1090
1091
1092
1093
1094
1095
1096
1097
1098
1099
1100
1101
1102
1103
1104
1105
1106
1107
1108
1109
1110
1111
1112
1113
1114
1115
1116
1117
1118
1119
1120
1121
1122
1123
1124
1125
1126
1127
1128

58. Hoechst, B. *et al.* A new population of myeloid-derived suppressor cells in hepatocellular carcinoma patients induces CD4(+)CD25(+)Foxp3(+) T cells. *Gastroenterology* **135**, 234-243 (2008).
59. Weiskirchen, R. *et al.* Genetic characteristics of the human hepatic stellate cell line LX-2. *PLoS One* **8**, e75692 (2013).
60. Clausen, B.E., Burkhardt, C., Reith, W., Renkawitz, R. & Forster, I. Conditional gene targeting in macrophages and granulocytes using LysMcre mice. *Transgenic Res* **8**, 265-277 (1999).
61. Agarwal, A. *et al.* Transient Opening of the Mitochondrial Permeability Transition Pore Induces Microdomain Calcium Transients in Astrocyte Processes. *Neuron* **93**, 587-605 e587 (2017).
62. Knier, B. *et al.* Myeloid-derived suppressor cells control B cell accumulation in the central nervous system during autoimmunity. *Nat Immunol* **19**, 1341-1351 (2018).
63. Du, P., Kibbe, W.A. & Lin, S.M. lumi: a pipeline for processing Illumina microarray. *Bioinformatics (Oxford, England)* **24**, 1547-1548 (2008).
64. Smyth, G. Limma: linear models for microarray data. . In: Gentleman, R., Carey, V., Huber, W., Irizarry, R. & Dudoit, S. (eds). *In Bioinformatics and computational biology solutions using R and Bioconductor*. Springer, 2005.
65. Tripathi, S. *et al.* Meta- and Orthogonal Integration of Influenza "OMICS" Data Defines a Role for UBR4 in Virus Budding. *Cell host & microbe* **18**, 723-735 (2015).
66. Bausch-Fluck, D. *et al.* A mass spectrometric-derived cell surface protein atlas. *PLoS ONE* **10**, e0121314 (2015).
67. Ahmed, N., Argirov, O.K., Minhas, H.S., Cordeiro, C.A.A. & Thornalley, P.J. Assay of advanced glycation endproducts (AGEs): surveying AGEs by chromatographic assay with derivatization by 6-aminoquinolyl-N-hydroxysuccinimidyl-carbamate and application to Nepsilon-carboxymethyl-lysine- and Nepsilon-(1-carboxyethyl)lysine-modified albumin. *Biochem J* **364**, 1-14 (2002).
68. Salomón, T. *et al.* Ketone Body Acetoacetate Buffers Methylglyoxal via a Non-enzymatic Conversion during Diabetic and Dietary Ketosis. *Cell Chemical Biology* **24**, 935-943.e937 (2017).

- 1129 69. Frank, O., Kreissl, J.K., Daschner, A. & Hofmann, T. Accurate determination of
1130 reference materials and natural isolates by means of quantitative (1)h NMR spectroscopy.
1131 *J Agric Food Chem* **62**, 2506-2515 (2014).
1132
1133

Figure 1

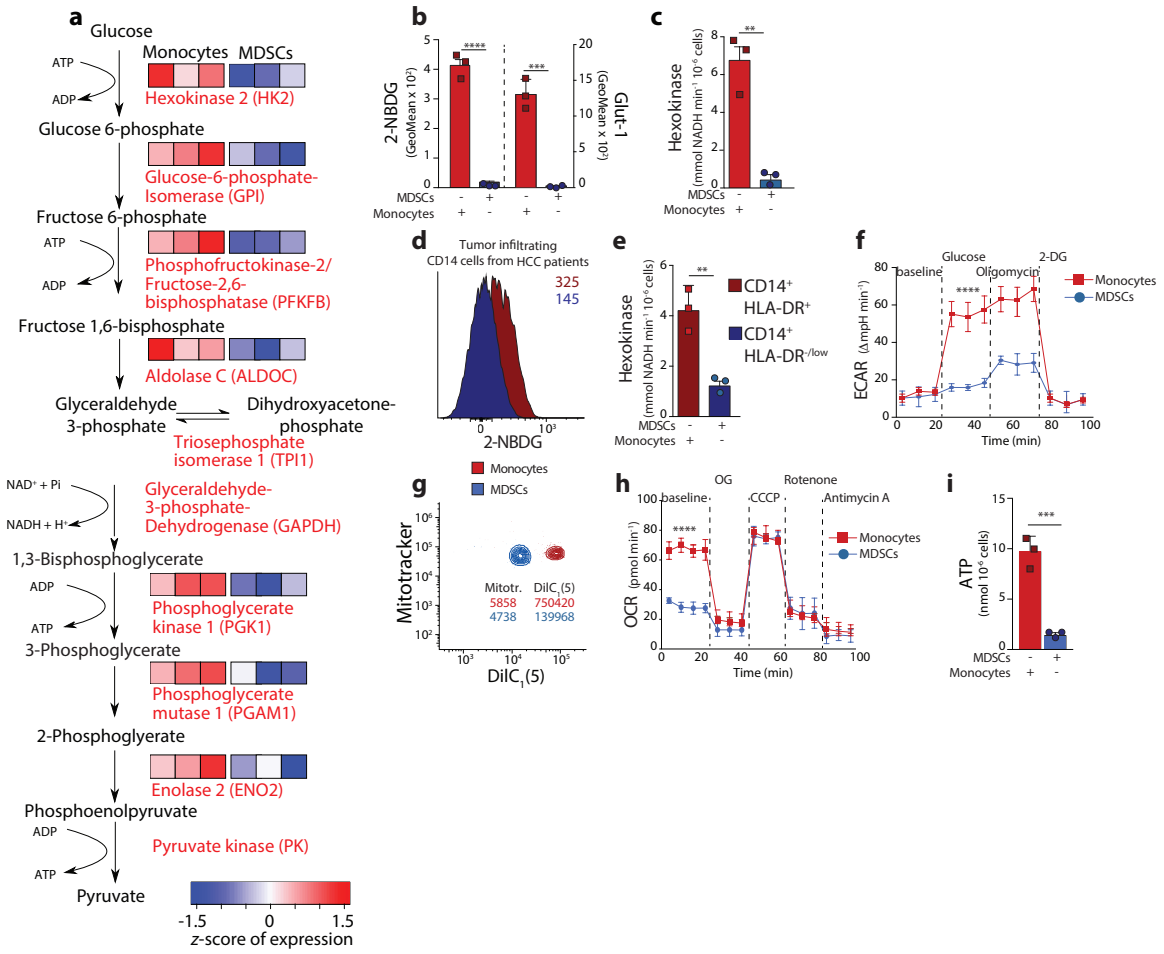


Figure 2

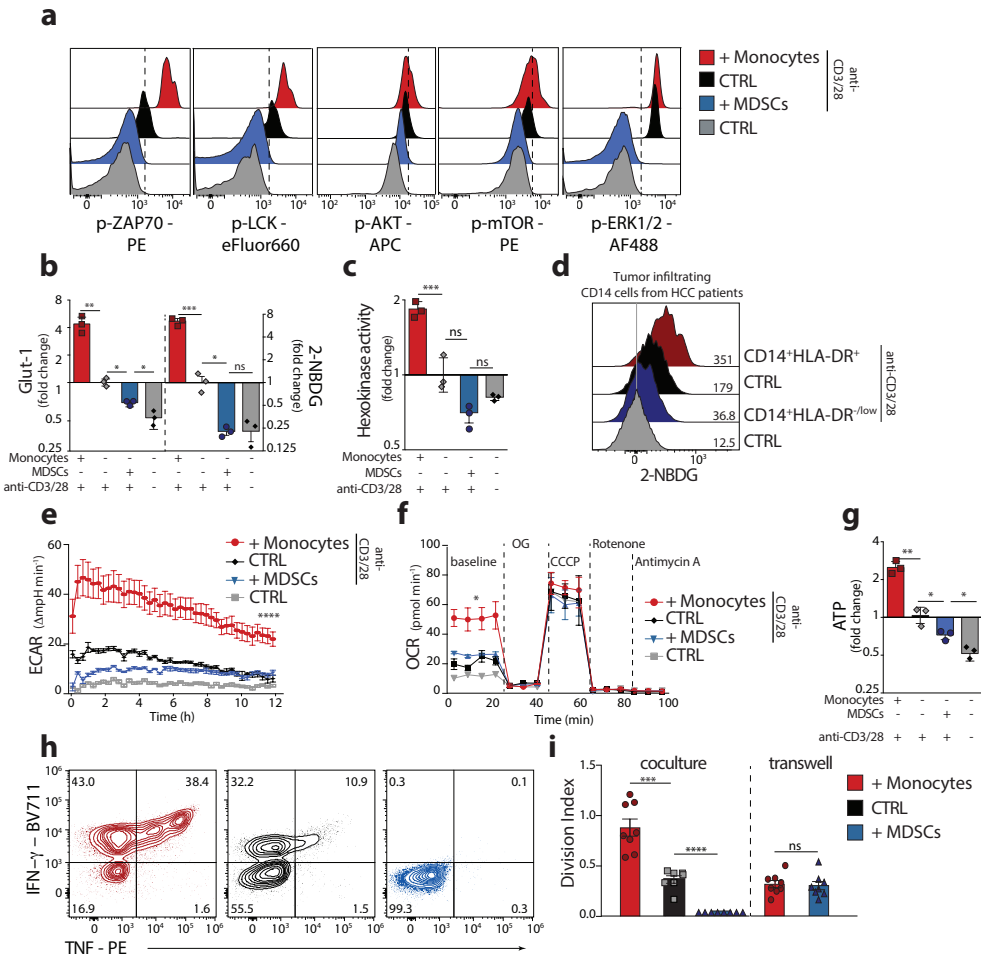


Figure 3

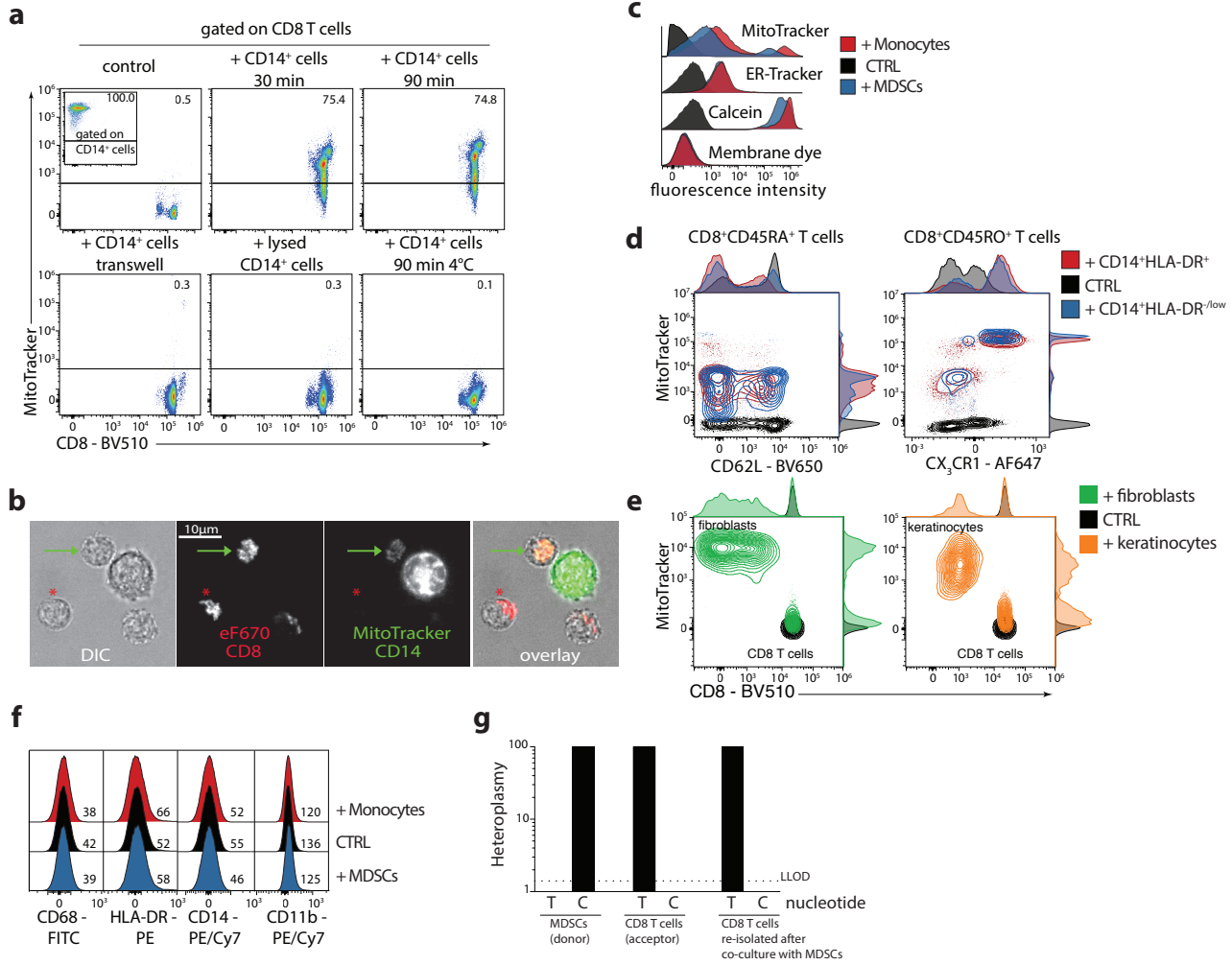


Figure 4

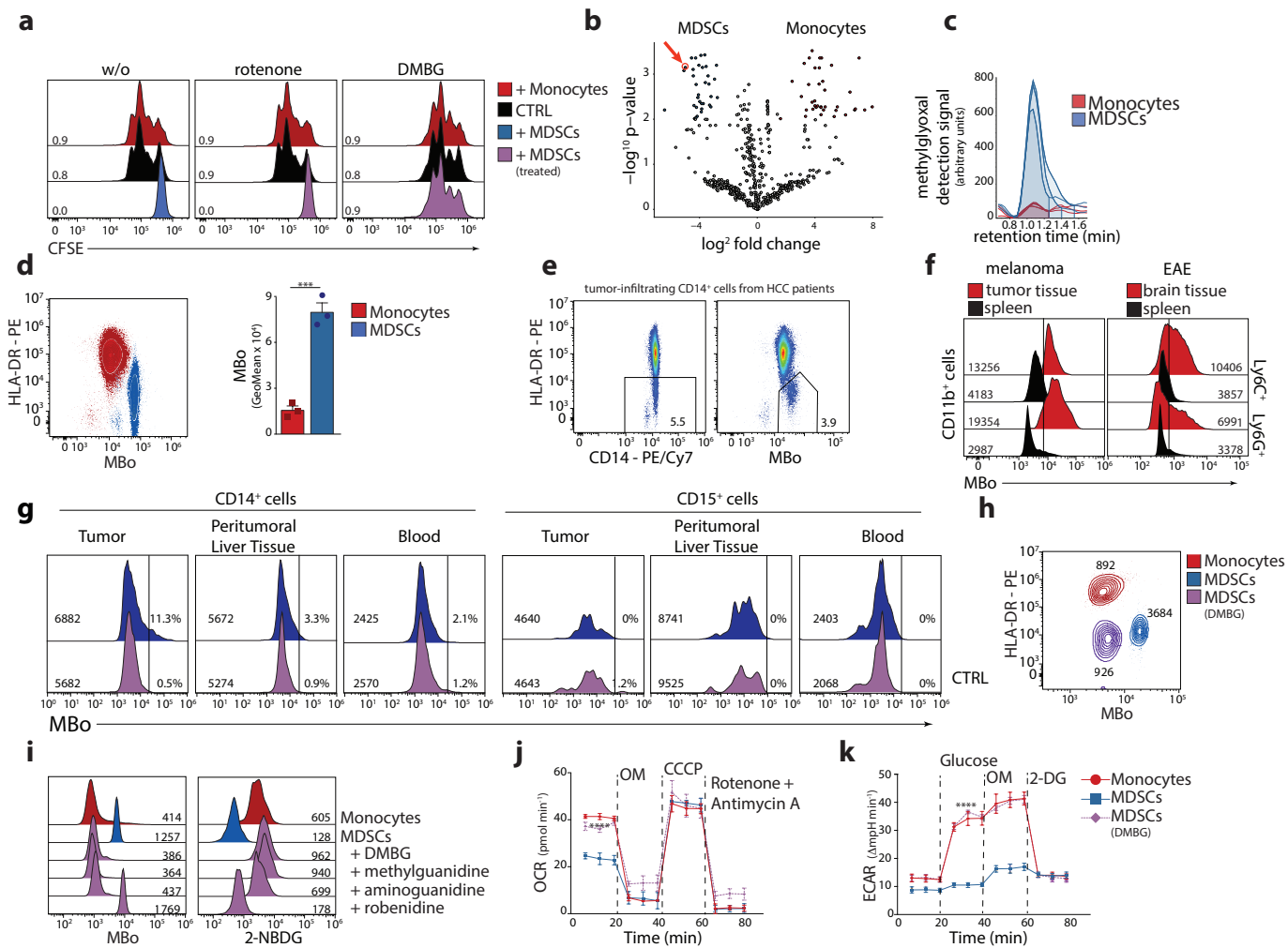


Figure 5

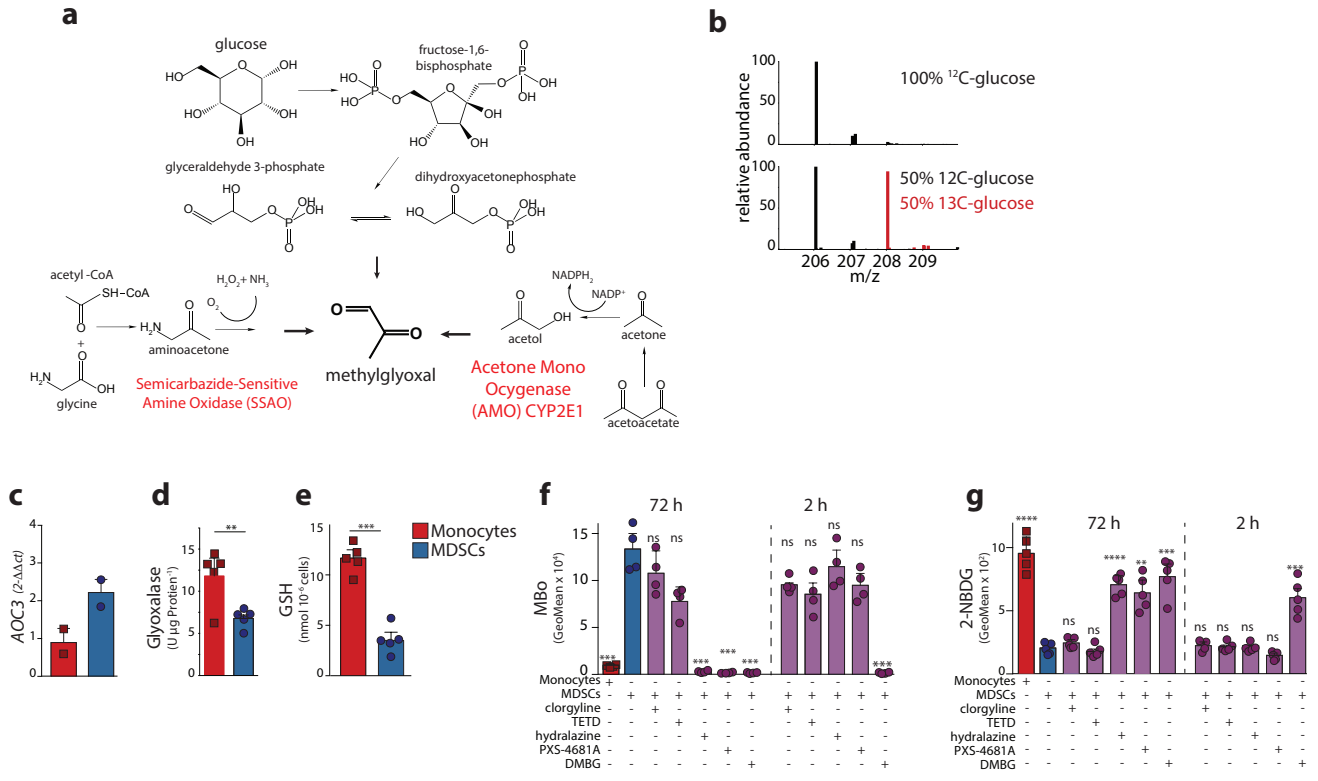


Figure 6

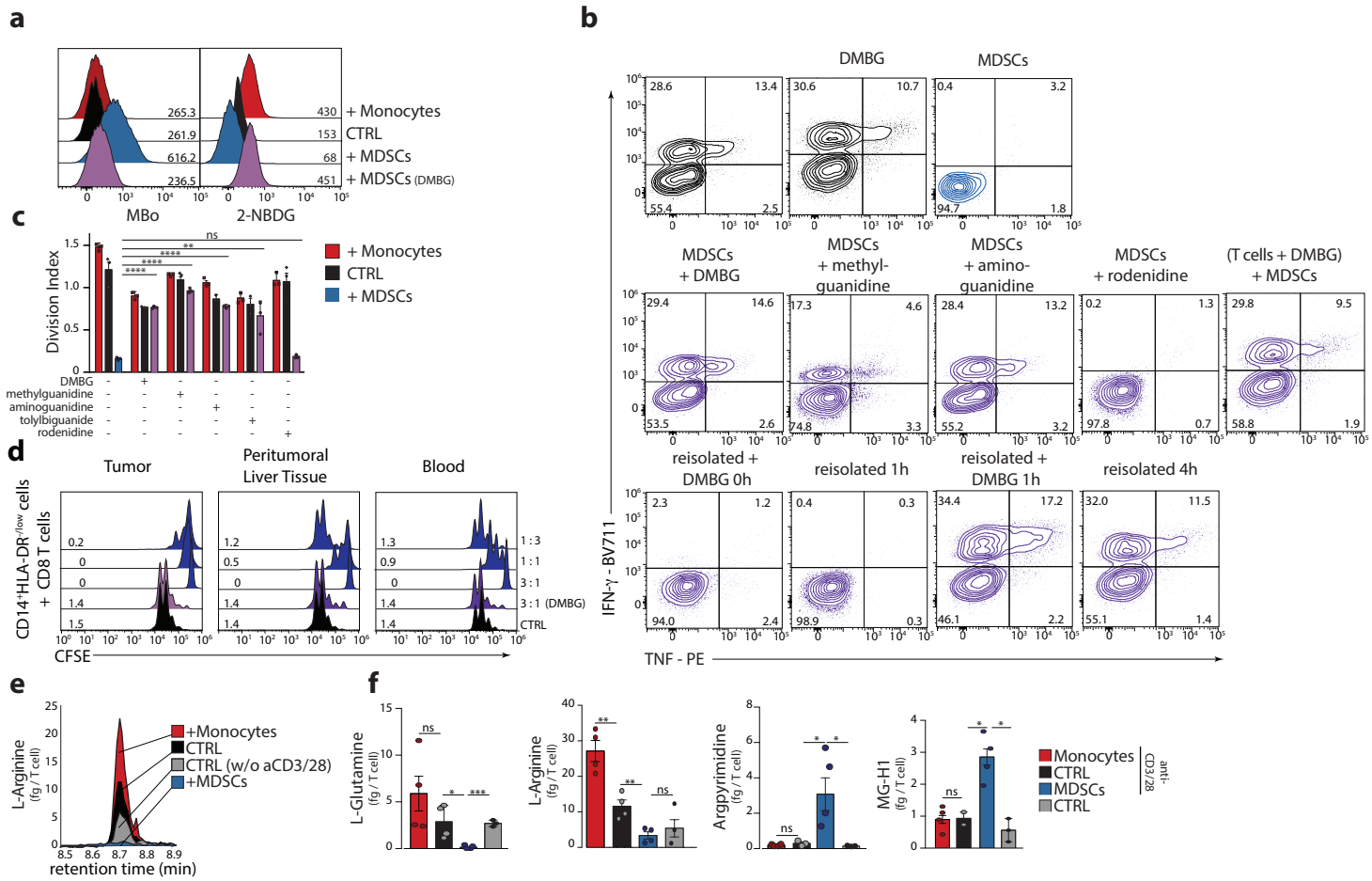
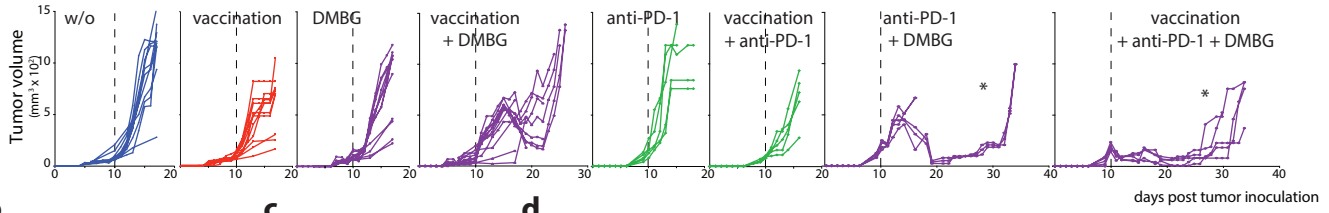
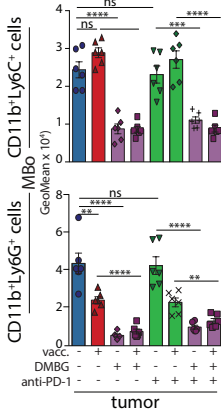


Figure 7

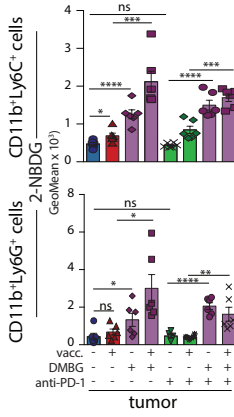
a



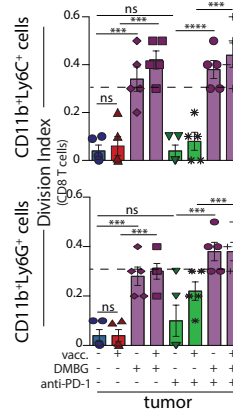
b



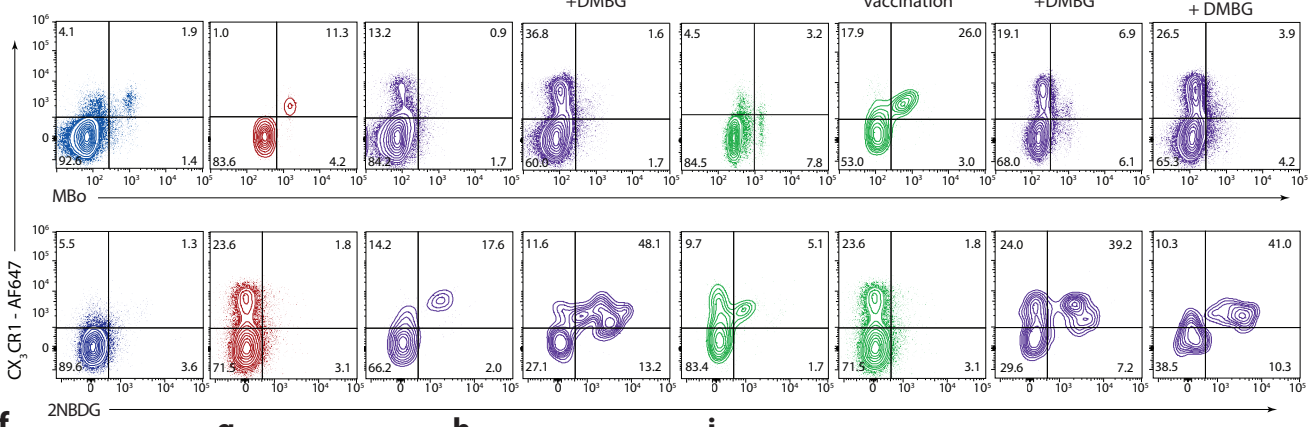
c



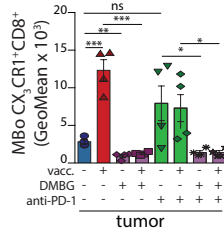
d



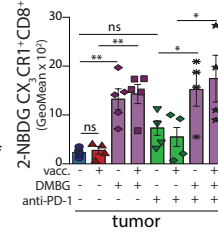
e



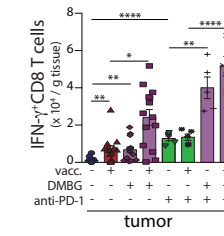
f



g



h



i

